Stability analysis of magnetic flux in thin-film superconductors

Dmitry Denisov

Thesis submitted for the degree of Philosophiae Doctor

Department of Physics

University of Oslo

October 2007

Series of dissertations submitted to the
Faculty of Mathematics and Natural Sciences, University of Oslo.
No. 659

ISSN 1501-7710

Cover: Inger Sandved Anfinsen.
Printed in Norway: AiT e-dit AS, Oslo, 2007.

Produced in co-operation with Unipub AS.
The thesis is produced by Unipub AS merely in connection with the
thesis defence. Kindly direct all inquiries regarding the thesis to the copyright
holder or the unit which grants the doctorate.

Unipub AS is owned by
The University Foundation for Student Life (SiO)

ACKNOWLEDGMENTS

This thesis is result of my work in the University of Oslo during last three years. These were good years of my life both in terms of work and study. I started to study the physics of superconductivity almost 8 years ago and I like it very much still. I'm really fascinated by effects and opportunities of superconductivity and it was my pleasure to be part of Superconductivity group at University of Oslo, one of the best group in this field.

I gain much knowledge and experience, even in topics which I never heard before. For this, first of all, I want to thank my supervisor Daniel Shantsev who helped me a lot in many ways during my time as PhD student. Discussions with him allowed me to find a new ways to solve physical problems. My other supervisor Yuri Galperin always amazed me with his ability to answer almost any question in any topics (not only in physics). Yuri always helped me to find a solution to some difficult questions – I'm grateful to him for that and also for his willingness to help at any time. I'm a theoretician myself so discussions with the head of our group Tom Johansen were very interesting for me because he examines problems from both theoretical and experimental points of view thus giving me new insights.

It was my pleasure to work in the Superconductivity Group with my fellow researchers. All of them are very friendly and responsive people. I thank Oleg Fefelov for helping me to find simple solution to one complicated problem. Vitaly Yurchenko always gave me good advices about various experiments. It was very interesting to discuss with Joakim Bergli, Jørn Inge Vestgården and Åge Andreas Falnes Olsen not only about physics but also about Norwegian culture, history and society. All of these people were also good companions during my travels abroad and around Norway on various conferences or just holiday trips.

I thank the interesting classes by professors Larissa Bravina and Knut Jørgen Måløy. Thanks to all my co-authors for our common projects and papers.

I want to express special thanks to professor Konstantin Tsendin. It was he who introduced me to world of scientific research when I was student back in State Technical University of Saint-Petersburg. I've started to deeply study superconductivity under his guidance. Konstantin Tsendin is good physicist, teacher and man, I'm glad that I was his student.

And besides physics I want to thank my family. I'm glad that I spend these enjoyable years in Oslo with my wife Anastasia and my daughter Varvara and I'm grateful for their support in all my doings and accomplishments.

CONTENTS

LIST OF PAPERS

Paper 1 D. V. Denisov, A. L. Rakhmanov, D. V. Shantsev, Y. M. Galperin and T. H. Johansen, ***Dendritic and uniform flux jumps in superconducting films***, Phys. Rev. B **73**, 014512 (2006).

Paper 2 D. V. Denisov, D. V. Shantsev, Y. M. Galperin, Eun-Mi Choi, Hyun-Sook Lee, Sung-Ik Lee, A. V. Bobyl, P. E. Goa, A. A. F. Olsen and T. H. Johansen, ***Onset of Dendritic Flux Avalanches in Superconducting Films***, Phys. Rev. Lett. **97**, 077002 (2006).

Paper 3 D. V. Denisov, D. V. Shantsev, Y. M. Galperin and T. H. Johansen, ***Flux saturation number of superconducting ring***, arXiv:0709.1086 [cond-mat.supr-con].

1. SHORT WORD ABOUT SUPERCONDUCTIVITY

This work presents theoretical results in the physics of superconductivity. The first part of the work is dedicated to the problem of thermomagnetic instabilities and flux avalanches in thin film superconductors. The second part describes the problem of flux trapped in the hole of the superconducting ring.

Superconductivity in general occupies very specific place in physics. Discovered in 1911 by Heike Kamerlingh Onnes it fast became one of the most intriguing phenomena. In superconducting state materials have zero electric resistance, which means that current can flow without any loss. In superconducting wire loops current can persist for years without any external support – such effects had been never seen before in classical physics. In fact superconductivity was one of the first quantum effects which can be observed in "classical world". Apart from zero-resistivity effect superconducting material almost totaly push-out magnetic field from its body. The other side of this effect is that magnets based on superconductors can create very high magnetic fields, which can never be achieved with conventional materials.

All these facts made superconductors very promising material for application in science, industry and even everyday life. However there is one serious drawback – superconductivity exists only at very low temperatures. In first discovered materials (Hg, Pb, Nb) the temperature of superconducting transition (T_c) was not higher than 20K, which is 250 degrees lower than temperature of water freezing. Of course this condition prevented wide spreading of superconductors.

However in 1986 high-temperature superconductor (HTSC) $LaBaCuO$ was discovered by Bednorz and Muller [1] with T_c around 40K. Lately more similar HTSCs were discovered with highest transition temperature around 160K (e.g. $HgBa_2Ca_2Cu_3O_9$ under pressure). It becomes very easy to study high-temperature superconductors with

help of the liquid nitrogen (very cheap coolant) which temperature is around 77K.

At present days application of superconductivity is spreading to different fields of science, industry, medicine and so on. There are still some drawbacks such as: working temperature is still far below zero and structure of HTSC materials is not well suited for industrial use. But nevertheless high-field superconducting magnets are widely used everywhere in industry. Super high-speed trains based on magnetic levitation works in several countries carrying passengers with speed up to 580 km/h. Extremely sensitive devices known as SQUIDs (Superconducting quantum interference devices) are used not only for research purposes but also in medicine for scanning electrical activity in the brain. High frequency generators for cell-phone industry are based on quantum effects in superconductors.

New materials with unique properties are still discovered after almost one hundred years since discovery of the first superconductors. One of such materials MgB_2 was discovered in 2001 [2]. Even with T_c only around 40K MgB_2 fast became very promising material because it is very easy to produce it and use in commercial applications. Besides application in nanoelectronics MgB_2 is used for production of superconducting wires. Some of these wires can be made up to 10km in length without any junction (Figure 1.1). Electrical current in such wires can be conducted without any losses at very large distances. There is even a plan to replace conventional wires with superconducting ones in several large cities .

To use superconductors in most efficient way we should carefully studied them in all aspects. For example it was found that at certain conditions (e.g. high magnetic fields) thermomagnetic instabilities can arise in superconducting device. From practical point of view this means loss of superconducting current, abrupt temperature increasing, magnetic noise and sometimes complete destruction of the device. During studies of such instabilities it was discovered that they can be in two forms: uniform and fingering-like, depending on the sample properties. Paper 1 and Paper 2 are dedicated to finding of conditions for development of these instabilities. We find the threshold magnetic field $H_{\text{fing}}(E, h_0)$ corresponding to arising to instability. Thin films are found to be much more unstable than bulk superconductors, and have a stronger tendency for

Fig. 1.1: Superconducting wire based on MgB_2. Black dots in the wire are MgB_2 itself, the rest is Cu surroundings. Maximum current of the wire at 27.5K – 330A. Standard batch length: in 2005 year - 1.6km, in 2006 year - 7km. Taken from site of COLUMBUS SUPERCONDUCTORS SPA (www.columbussuperconductors.com).

formation of fingering (dendritic) pattern. All these studies and results are presented in Chapter 2. At the end of the Chapter 2 we give possible solution how to completely avoid instability in the sample (e.g. MgB_2).

Another interesting problem in physics of superconductivity is flux trapping. By controlling the motion of magnetic vortices with help of asymmetric pinning in the sample one can remove unwanted trapped flux in devices or even guide vortices in chosen direction. By creating special arrays of dots and antidots which serve as pinning sites in the sample it is possible to trap large quantity of magnetic flux quanta without destruction of superconducting state. This allows to use superconductors in higher magnetic fields increasing the range of their possible applications. Most of such experiments were performed on thin-film superconductors. Many models were proposed how to guide vortices and which geometry of antidots must be used. But all these models are based on the fact that artificial hole can trap magnetic flux. However no answer had been given to the general problem - how many vortices can be trapped by one hole in thin superconducting film. In Chapter 3 the solution to this problem is shown. We found how many flux quanta can be trapped in thin superconducting ring. We also compare this result for thin-films with the similar answer obtained for bulk superconductors.

2. THERMOMAGNETIC INSTABILITIES

2.1 General description of the phenomena

Phenomena that create intriguing traces of activity that can be observed by direct visual methods are among the most fascinating things in nature. Penetration of magnetic flux in type-II superconductors seen by magneto-optical (MO) imaging is one example, where spectacular dendritic flux patterns occurs in superconducting films (Figure 2.1).

The phenomenon has been observed in a large number of materials: $YBa_2Cu_3O_x$, Nb, MgB_2, Nb_3Sn, NbN, YNi_2B_2C and Pb [3–9] (all films). All of them show essentially the same characteristic behavior. In abrupt bursts the film becomes invaded by flux in narrow finger-like regions that often form a complex and sample-spanning dendritic structure. These sudden events occur typically during a slow ramping of the applied magnetic field, and at temperatures below a certain fraction of the superconducting transition temperature T_c. It is also characteristic that the flux patterns are never reproduced when experiments are repeated (Figure 2.2), thus ruling out possible explanations based on material defects guiding the flux motion. The massive experimental data existing today [3–17] indeed suggest that the phenomenon is a generic instability of the vortex matter in superconducting films. The emerging dendritic patterns are reminiscent of those formed during the crystal growth [18], viscous fluid flow [19] and electric discharge [20].

Dendrites can look very fascinating but their appearance in the sample means thermomagnetic instability . Such instabilities can be the reason for huge magnetic noises, they reduce the effective critical current density and even can lead to total malfunction of the superconducting device. Because of these reasons such instabilities

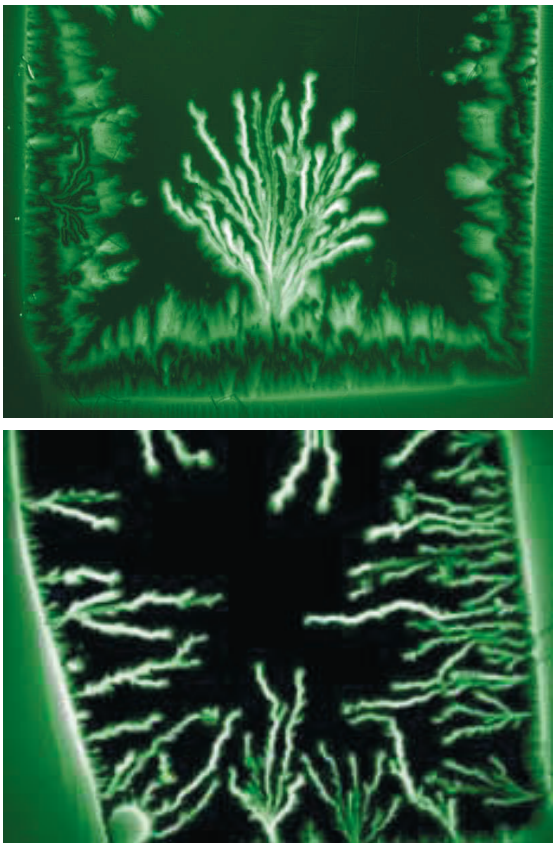

Fig. 2.1: Various images of dendrites in MgB_2. Bright green color corresponds to magnetic field penetrated into body of superconductor. The dendrites were formed at applied field 17mT and temperature 9.9K. Pictures are taken from the internet site of Superconductivity Laboratory at the University Oslo (http://www.fys.uio.no/super/).

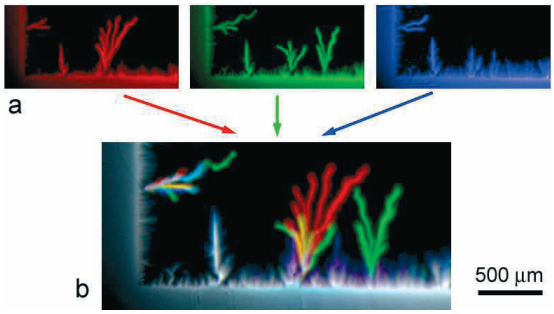

Fig. 2.2: (a) Three MO images of flux penetration in MgB_2 taken during repeated identical experiments. (b) Image obtained by adding the 3 complementary colored images above. In the sum image the grey tone regions are those of repeated behavior, whereas colors show where there is no or only partial overlap. Strong irreproducibility is seen in the dendrite shapes, while the penetration near the edge and along static defects is reproducible. The dendrites tend to nucleate at preferred sites along the edge, which is due to small edge cavities giving local field amplification. The experiments were performed after cooling to 9.2 K and applying a magnetic field of 20 mT.

must be avoided in most superconducting applications.

2.2 Experimental setup

There are many methods to observe magnetic field penetration into superconductor. However method used in Superconductivity Laboratory at University of Oslo is one of the most fascinating. Method of Magneto-Optical imaging allows to actually "see" (with help of microscope or digital camera) how magnetic field distributed in the superconductor. This method based on well known Faraday effect, i.e., rotation of the plane of polarized light in the Faraday-active crystal induced by magnetic field. On 13 September, 1845, Michael Faraday wrote in his diary "...magnetic force and light were proved to have relation to each other. This fact will most likely prove exceedingly fertile and of great value in the investigation of both conditions of natural force". A number of different materials have been applied as indicators in MO imaging: cerous nitrate-

glycerol [21], various europium compounds (EuS, EuSe) [22] and bismuth-substituted iron garnets [23]. Today, the most popular indicator is the ferri-magnetic $Bi : YIG$ film with in-plane spontaneous magnetization [24]. Application of a perpendicular magnetic field creates an out-of-plane component of the magnetization responsible for the Faraday rotation. A single-crystal film with typical thickness of a few microns can be grown by liquid-phase epitaxy on a gadolinium-gallium-garnet (GGG) substrate. The Magneto-Optical indicator (made of Faraday-active crystals) is placed in the light beam path between a polarizer and an analyzer crossed by 90 degrees. If a magnetic field is present perpendicularly to the film, the magnetization of the $Bi : YIG$ will be tilted out of the plane. The perpendicular component of the magnetization will cause a Faraday rotation of the light. The rotation angle will be small where the magnetic field is small, and large in regions of high fields. After leaving the analyzer the light will therefore have an intensity distribution that reflects the magnitude of the field in the plane of the indicator film (Figure 2.3).

Using magneto-optical technique one able to see the general picture of flux penetration in the sample with size around several mm. Moreover it is also possible to visualize single vortices with size of several μm in the flux front (specific samples must be used for this task). One can even see the Abrikosov lattice formed by these vortices (Figure 2.4) or how vortices enters the sample and move with increasing magnetic field.

2.3 Model and basic equations

The dendrites is commonly observed at low temperatures in type-II superconductor films with strong pinning [25–28]. Experimentally dendrites always occurs in thin films only, however thermomagnetic instability in general can also develop in bulk superconductors.

Let's begin with general picture of instability process in superconductor. It is the nature of superconductor material to totally push magnetic field from its body. Magnetic field penetrates the superconductor only in very thin skin layer, the depth of penetration is commonly designated as λ_L. However if we apply high enough magnetic

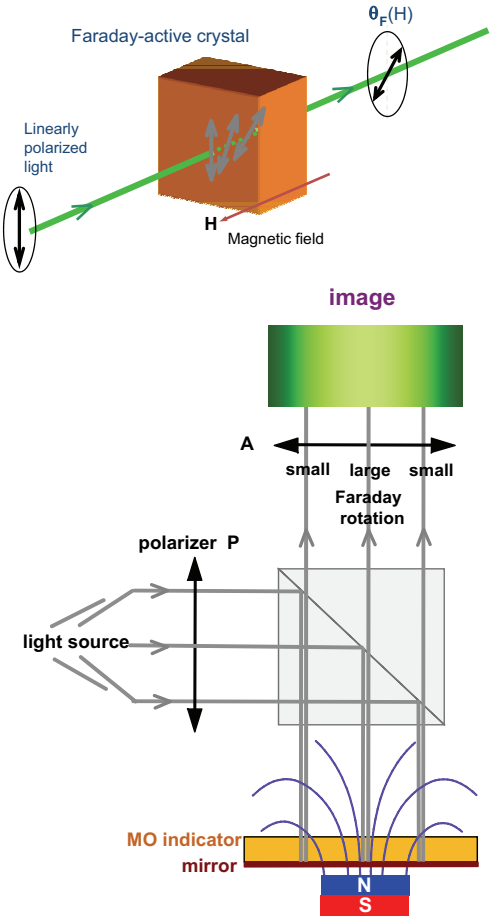

Fig. 2.3: Schematic description of Faraday-active crystal and Magneto-Optical Imaging experimental setup. Pictures are taken from the internet site of Superconductivity Laboratory at the University Oslo (http://www.fys.uio.no/super/).

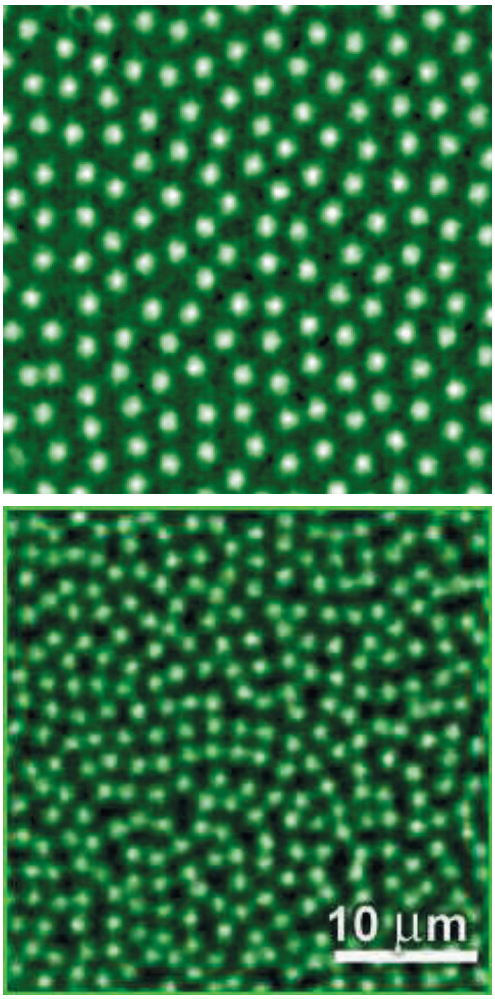

Fig. 2.4: Magneto-optical images of vortices in a $NbSe_2$ superconducting crystal at 4.3 K after cooling in magnetic field of 3 and 7 Oe [5].

field it will begin to further penetrate the superconductor. For type-II superconductors this leads to destruction of superconducting state in the region where magnetic field entered the sample. It also should be noted that this penetration process is quantized as was discovered by Abrikosov [29]. The field enters the superconductor in the form of small vortices each carrying one flux quantum $\Phi_0 = h/2e$. These vortices do not move freely inside the sample because they pinned by microscopic inhomogeneities which naturally exist in the material or artificially created. In the vortex free region superconductivity still exists. But application of even higher magnetic field can lead to depining and motion of vortices. The motion of vortices releases energy, and hence increases the local temperature. The temperature rise reduces flux pinning, and facilitates further vortex motion. As a result it will be more easier for magnetic field to penetrate the superconductor in the given region, which means more vortex motion and more heat dissipation. Such positive feedback loop leads to formation of abrupt flux avalanches [25,27], and consequently to thermal runaways and abrupt field penetration.

However, why such avalanches should develop into dendritic patterns was a topic under vivid discussion, and several competing theories were proposed. They include a stability analysis taking into account the complex non-local electrodynamics of thin film superconductors (Paper 1 and [30]), a boundary layer model assuming shape-preserving fronts [31], and a shock wave approach [32], all leading to substantially different predictions. It is shown that the model proposed in this thesis (Paper 1) provides an excellent quantitative description of key features. One of such features is the instability threshold field H_{fing} – the magnetic field when the first avalanche occurs, within our model we can also predict how H_{fing} depends on both temperature and the sample size.

The first theories [25,26] which were developed for description of avalanche processes could only explain "uniform flux jumps". The uniform instability starts simultaneously in a large area near edge of the sample and then one enormous "uniform flux jump" occurs containing several thousands of vortices with smooth and essentially straight flux front. This picture was observed experimentally in a bulk superconductors. However for certain conditions the instability can develop much more differently. Numerous

experiments [3–15,33,34] confirms that magnetic field can penetrate the superconductor in the form heavily branched "dendritic" patterns.

The pattern of each dendritic instability can differ much from each other depending on the material and quality of the sample (and substrate) and parameters of the system (temperature, applied electromagnetic fields and so on). It was already stated (Figure 2.2) that even with the same parameters process of dendrites formation can be completely random. It is very hard to describe the development of such process but is possible to find conditions for its initial start. The model presented here describes initial conditions for thermomagnetic instability.

Initially the problem of flux pattern was examined in the *slab* geometry [35]. Experimentally, however, the dendritic flux patterns are mostly observed in *thin film* superconductors placed in a perpendicular magnetic field. A first analysis of this perpendicular geometry was published by Aranson *et al.* [30]. In this chapter we present more exact and complete picture of the dendritic instability and analyze the criteria of its realization.

In the following we restrict ourselves to a conventional linear analysis [25, 26, 36] of the instability and consider the space-time development temperature T. In contrast to the slab case [35], the heat transfer from the superconductor to a substrate as well as the nonlocal electrodynamics in thin films are taken into account. Consequently, the results depend significantly on the heat transfer rate h_0, as well as on the film thickness d. Our main result is that the instability in the form of narrow fingers perpendicular to the background field $\mathbf{E}$ occurs much easier in thin films than in slabs and bulk samples, and the corresponding threshold field E_c is found to be proportional to the film thickness d.

Consider the perpendicular geometry shown in Figure 2.5, with a thin superconducting strip placed in a transverse magnetic field, $\mathbf{H}$. The strip is infinite along the y axis, and occupies the space from 0 to d in the z-direction and from 0 to $2w$ in the x-direction. It is assumed that $d \ll w$. In the unperturbed state the screening current flows along the y-axis.

The distributions of the current density $\mathbf{j}$ and magnetic induction $\mathbf{B}$ in the flux

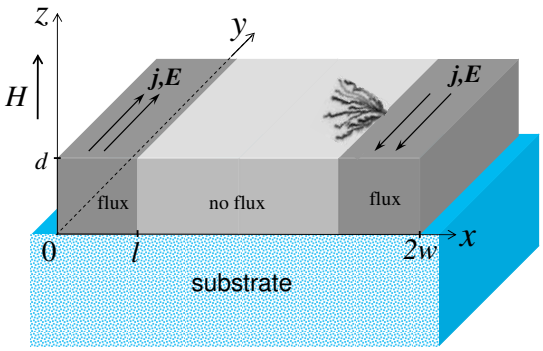

Fig. 2.5: A superconductor strip on a substrate. The dark gray area is the flux-penetrated region.

penetrated region $0 < x < \ell$ are determined by the Maxwell equation

$$\text{curl } \mathbf{B} = \mu_0 \mathbf{j}\,, \tag{2.1}$$

where the common approximation $\mathbf{B} = \mu_0 \mathbf{H}$ is used. To find the electric field and the temperature we use another Maxwell equation together with the equation for thermal diffusion,

$$\text{curl } \mathbf{E} = -\partial \mathbf{B}/\partial t\,, \tag{2.2}$$

$$C(\partial T/\partial t) = \kappa \nabla^2 T + \mathbf{jE}\,. \tag{2.3}$$

Here C and κ are the specific heat and thermal conductivity, respectively.

Equations (2.1)-(2.3) should be supplemented by a current-voltage relation $j = j(E, B, T)$. For simplicity we assume a current-voltage curve of the form

$$\mathbf{j} = j_c(T) g(E)\, (\mathbf{E}/E)\,. \tag{2.4}$$

A strong nonlinearity of the function $g(E)$ leads to formation of a quasi-static critical state with $j \approx j_c(T)$, where j_c is the critical current density [37]. We neglect any B-dependence of j_c, i. e., adopt the Bean model. The exact form of $g(E)$ is not crucially important, the only issue is that it represents a very steep $E(j)$ curve having a large logarithmic derivative,

$$n(E) \equiv \partial \ln E / \partial \ln j \approx j_c/\sigma E \gg 1\,. \tag{2.5}$$

Here σ is the differential electrical conductivity, $\sigma(E) \equiv \partial j/\partial E$. The parameter n generalizes the exponent in the frequently used power-law relation $E \propto j^n$ with n independent of E.

The key dimensionless parameter of the model is the ratio of thermal and magnetic diffusion coefficients [25]:

$$\tau \equiv \mu_0 \kappa \sigma / C \,. \tag{2.6}$$

The smaller τ is, the slower heat diffuses from the perturbation region into the surrounding areas. Hence, one can expect that for smaller τ: (i) the superconductor is more unstable, and (ii) the formation of instability-induced nonuniform structures is more favorable.

In the following we assume that the strip is thinner than the London penetration depth, λ_L, and at the same time much wider than the effective penetration length, $\lambda_{\text{eff}} = \lambda_L^2/d$,

$$d \le \lambda_L \ll \sqrt{dw} \,.$$

The stationary current and field distributions in a thin strip under such conditions were calculated by several authors [38–40], finding that the flux penetration depth ℓ is related to the applied field by the expression

$$\ell \,/\, w \;=\; \pi^2 H^2 / 2 d^2 j_c^2 \tag{2.7}$$

Here it is assumed that the penetration is shallow, or more precisely that $\lambda_{\text{eff}} \ll \ell \ll w$.

2.4 Perturbation analysis

We seek solutions of equations (2.1)-(2.4) in the form

$$T + \delta T(x,y,z,t), \quad \mathbf{E} + \delta \mathbf{E}(x,y,z,t), \quad \mathbf{j} + \delta \mathbf{j}(x,y,z,t)$$

where T, $\mathbf{E}$ and $\mathbf{j}$ are background values. The background electric field may be created, e.g., by ramping the external magnetic field, and for simplicity we assume it to be coordinate independent. Allowing for such a dependence would only lead to insignificant numerical corrections, as discussed in [35]. Similarly, we will assume a uniform background temperature.

Whereas it follows from symmetry considerations that $E_x = 0$, both components of the perturbation $\delta\mathbf{E}$ will in general not vanish. Linearizing the current-voltage relation, Eq. (2.4) one obtains:

$$\delta\mathbf{j} = \left(\frac{\partial j_c}{\partial T}\,\delta T + \sigma\,\delta E_y\right)\frac{\mathbf{E}}{E} + j_c\frac{\delta\mathbf{E}_x}{E}\,. \tag{2.8}$$

We shall seek perturbations in the form

$$\begin{aligned}
\delta T &= T^*\theta\exp(\lambda t/t_0 + ik_x\xi + ik_y\eta)\,,\\
\delta E_{x,y} &= E\varepsilon_{x,y}\exp(\lambda t/t_0 + ik_x\xi + ik_y\eta)\,,\\
\delta j_{x,y} &= j_c i_{x,y}\exp(\lambda t/t_0 + ik_x\xi + ik_y\eta)\,,
\end{aligned} \tag{2.9}$$

where θ, ε and i are z-dependent dimensionless Fourier amplitudes. The coordinates are normalized to the adiabatic length $a = \sqrt{CT^*/\mu_0 j_c^2}$, where $T^* = -(\partial \ln j_c/\partial T)^{-1}$ is the characteristic scale of the temperature dependence of j_c, so that $\xi = x/a$, $\eta = y/a$, $\zeta = z/a$. The time is normalized to $t_0 = \sigma CT^*/j_c^2 = \mu_0\sigma a^2$, which is the magnetic diffusion time for the length a. $\mathrm{Re}\,\lambda$ is the dimensionless instability increment, which when positive indicates exponential growth of the perturbation.

We can now use the formulas (2.9) to rewrite the basic equations in dimensionless variables. From Eq. (2.8) one finds for the components of the current density perturbation $\mathbf{i}$,

$$i_x = \varepsilon_x\,, \quad i_y = -\theta + n^{-1}\varepsilon_y\,. \tag{2.10}$$

Combining the Maxwell equations (2.1) and (2.2), and the thermal diffusion equation (2.3) yields

$$\mathbf{k}\times[\mathbf{k}\times\varepsilon] = \lambda n\,\mathbf{i}\,, \tag{2.11}$$

$$\lambda\theta = \tau\left(-k_y^2\theta + \frac{\partial^2\theta}{\partial\zeta^2}\right) + (i_y + \varepsilon_y)/n\ . \tag{2.12}$$

In components, equation (2.11) reads as

$$ik_y\left(\frac{\partial\varepsilon_y}{\partial\xi} - ik_y\varepsilon_x\right) - \frac{\partial^2\varepsilon_x}{\partial\zeta^2} = -\lambda n\varepsilon_x\,, \tag{2.13}$$

$$\frac{\partial}{\partial\xi}\left(\frac{\partial\varepsilon_y}{\partial\xi} - ik_y\varepsilon_x\right) + \frac{\partial^2\varepsilon_y}{\partial\zeta^2} = \lambda n f(\lambda,k_y)\varepsilon_y\,, \tag{2.14}$$

$$\frac{\partial}{\partial\zeta}\left(\frac{\partial\varepsilon_x}{\partial\xi} + ik_y\varepsilon_y\right) = 0\,. \tag{2.15}$$

Magneto-optical imaging shows that flux patterns produced by the dendritic instability [3–15, 33, 34] are characterized by having $k_y \gg k_x$. Therefore, we have neglected the heat flow along x direction compared to that along the y direction. Later we will check the consistency of this assumption by showing that indeed the fastest growing perturbation has $k_y \gg k_x$.

2.5 Boundary conditions

We assume that heat exchange between the superconducting film and its environment follows the Newton cooling law. For simplicity we let the boundary condition, $\kappa\nabla(T+\delta T) = -h_0(T+\delta T-T_0)$, apply to both film surfaces. Here T_0 and h_0 are the effective environment temperature and heat transfer coefficient, respectively. Eqs. (2.10) and (2.12) can now be integrated over the film thickness to yield:

$$\theta = \frac{(1+n^{-1})\varepsilon_y}{n\lambda + n\tau(k_y^2+h)+1}\,, \tag{2.16}$$

where

$$h = 2h_0a^2/\kappa d\,. \tag{2.17}$$

In the remaining part of the paper we let θ, ε and $\mathbf{i}$ denote perturbations averaged over the film thickness.

We seek a solution of the electrodynamic equations in the flux penetrated region, $0 \le \xi \le \ell/a$. At the film edge, $\xi = 0$, one has $\delta j_x = 0$ and, consequently, $\delta E_x = 0$. In the Meissner state both the electric field and heat dissipation are absent, so that $\delta E_y = \delta T = \delta j_y = 0$ at the flux front, $\xi = \ell/a$. Thus, the Fourier expansions for the x and y components of electric field perturbation will contain only $\sin(k_x\xi)$ and $\cos(k_x\xi)$, respectively. Then the boundary conditions are satisfied for

$$k_x = (\pi a/2\ell)\,(2s+1)\,, \quad s = 0, 1, 2, \ldots\,.$$

Since ℓ depends on magnetic field, the values of k_x are also magnetic field dependent.

Now we can integrate Eq. (2.11) over the film thickness and employ the symmetry

of the electrodynamic problem with respect to the plane $z = d/2$. It yields

$$\begin{aligned} -ik_y(k_x\varepsilon_y + ik_y\varepsilon_x) - \frac{2a}{d}\varepsilon'_x &= -\lambda n\varepsilon_x, \\ -k_x(k_x\varepsilon_y + ik_y\varepsilon_x) + \frac{2a}{d}\varepsilon'_y &= -\lambda n f(\lambda, k_y)\varepsilon_y\,. \end{aligned} \tag{2.18}$$

We have here introduced the function

$$f(\lambda, k_y) \equiv \frac{i_y}{\varepsilon_y}\frac{1}{n} - \frac{1+n^{-1}}{n\lambda + n\tau(k_y^2+h)+1}\,.$$

Note that the equation for the z-component of the field is satisfied automatically. The derivatives $\varepsilon'_{x,y}$ with respect to ζ are taken at the film surface, $\zeta = d/2a$. To calculate them, one needs the electric field distribution outside the superconductor, where the flux density is given by the Bio-Savart law,

$$\mathbf{B}(\mathbf{r}) = \mu_0\mathbf{H} + \frac{\mu_0}{4\pi}\int d^3\mathbf{r}'\,\frac{\mathbf{j}\times(\mathbf{r}-\mathbf{r}')}{|\mathbf{r}-\mathbf{r}'|^3}\,.$$

The perturbation of flux density is then,

$$\delta B_{x,y} = \pm\mu_0\zeta d\int_0^{\ell/a} d\xi' \int_{-\infty}^{\infty} d\eta' G(\xi-\xi', \eta-\eta')\delta j_{y,x},$$
$$G(\xi,\eta) = \frac{1}{4\pi\left(\xi^2+\eta^2+(d/2a)^2\right)^{3/2}}.$$

Here we have approximated the average over ζ' substituting $\zeta' = 0$. In this way we omit only terms of the order of $(d/a)^2 \ll 1$. The integration over ξ' should, in principle, cover also the Meissner region, $\xi' > l/a$. Though the flux density there remains zero during the development of perturbation, the Meissner current will be perturbed due to the nonlocal current-field relation. However the kernel $G(\xi,\eta)$ decays very fast at distances larger than d/a and therefore the Meissner current perturbation produces only insignificant numerical corrections.

The perturbation of magnetic field can be related to that of electrical field by Eq. (2.2), which can be rewritten as

$$\delta E'_{x,y}/E = \mp\lambda n\,\delta B_{y,x}/\mu_0 a j_c\,. \tag{2.19}$$

Due to continuity of the magnetic field tangential components Eq. (2.19) is also valid at the film surface, $\zeta = d/2a$. Thus it can be substituted into Eq. (2.18). The Fourier

components of the kernel function $G(\xi,\eta)$ with respect to η can be calculated directly yielding

$$G(\xi,k_y)=\frac{k_y a}{2\pi\ell}\cdot\frac{\mathrm{K}_1\left(k_y\sqrt{\xi^2+(d/2a)^2}\right)}{\sqrt{\xi^2+(d/2a)^2}} \tag{2.20}$$

where K_1 is the modified Bessel function of the second kind.

The above Fourier expansions in $\cos(k_x\xi)$ and $\sin(k_x\xi)$ correspond to the finite interval $-2\ell/a<\xi<2\ell/a$. Therefore we should continue $\varepsilon_{x,y}$ from $0<\xi<\ell/a$ to this interval and then introduce G_x and G_y as analytical continuations of $G(\xi-\xi',k_y)$ having the same symmetry as ε_x and ε_y, respectively (see Appendix A for details). All this allows us to rewrite the set (2.18) as

$$\begin{aligned}
&-ik_xk_y\varepsilon_y+(k_y^2+\lambda n)\varepsilon_x\\
&\qquad=(d/2a)\lambda n\sum_{k_x'}G_x(k_x,k_x',k_y)\varepsilon_x(k_x')\,, &(2.21)\\
&(k_x^2+\lambda nf)\varepsilon_y+ik_xk_y\varepsilon_x\\
&\qquad=(d/2a)\lambda nf\sum_{k_x'}G_y(k_x,k_x',k_y)\varepsilon_y(k_x')\,, &(2.22)\\
&\left\{\begin{array}{c}G_x(k_x,k_x',k_y)\\G_y(k_x,k_x',k_y)\end{array}\right\}=4\int_0^{\ell/a}d\xi\int_0^{\ell/a}d\xi' G(\xi-\xi',k_y)\\
&\qquad\times\left\{\begin{array}{c}\sin(k_x\xi)\sin(k_x'\xi')\\\cos(k_x\xi)\cos(k_x'\xi')\end{array}\right\}. &(2.23)
\end{aligned}$$

We are interested only in the specific case of very thin strip,

$$\alpha=d/2\ell\ll 1\,. \tag{2.24}$$

One can then find analytical expressions for the kernel, and it turns out that only its diagonal part, $k_x=k_x'$, is important. In this manuscript we present analytical expressions up to the first order in α, while the plots are calculated up to the second order. The second-order analytical expressions along with detailed description of kernel G (2.23) are shown in Appendix A. The kernel (2.23) can be written as

$$G_{x,y}(k_x,k_x,k_y)=\frac{a}{\ell}\left[\frac{1-\gamma(\alpha,k_x)\alpha}{\alpha}\right], \tag{2.25}$$

where $\gamma(\alpha, k_x)$ is a dimensionless function. In what follows we shall consider only the main instability mode, $k_x = \pi a/2\ell$, which turns out always to be the most unstable one. For this mode, and in the limit $\alpha \to 0$, the function $\gamma(\alpha, k_x)$ approaches a constant value ≈ 5.

Substituting the above expression for G into Equations (2.21) and (2.22) one obtains the dispersion relation for $\lambda(k_x, k_y)$:

$$A_1\lambda^2 + A_2\lambda + A_3 = 0\,. \tag{2.26}$$

Here

$$A_1 = n\gamma\alpha\,, \quad A_2 = k_y^2(1+\tau A_1) + nk_x^2 + A_1(h\tau - 1)\,,$$
$$A_3 = k_y^4\tau + nk_x^2k_y^2\tau + nk_x^2(h\tau + 1/n) + k_y^2(h\tau - 1).$$

2.6 Threshold values of electric and magnetic fields

Let us first consider the simple case of a uniform perturbation, $k_y = 0$. One finds from Eq. (2.26) that the perturbation will grow ($\mathrm{Re}\,\lambda > 0$) if

$$h\tau < 1 - k_x^2/\gamma\alpha\,. \tag{2.27}$$

When the flux penetration region, ℓ, is small, i. e., k_x is large, the system is stable. As the flux advances, k_x decreases, and the system can eventually become unstable. The instability will take place, however, only if $h\tau < 1$. Otherwise the superconducting strip of any width will remain stable no matter how large magnetic field is applied. This size-independent stability means that at $h\tau \geq 1$ the heat dissipation due to flux motion is slower than heat removal into the substrate.

Equation (2.27) further simplifies in the adiabatic limit, $\tau \to 0$, when the heat production is much faster than heat diffusion within the film or into the substrate. The instability then develops at $k_x^2/(\gamma\alpha) < 1$, which in dimensional variables reads as $\mu_0 j_c^2 ld > CT^*(\pi^2/2\gamma)$. Assuming small penetration depth, $l \ll w$, and using Eq. (2.7) this criterion can be rewritten as $H > H_{\mathrm{adiab}}$, with the adiabatic instability field,

$$H_{\mathrm{adiab}} = \sqrt{\frac{d}{w}\,\frac{CT^*}{\gamma\mu_0}} \sim \sqrt{\frac{d}{w}}\;H_{\mathrm{adiab}}^{\mathrm{slab}}\,. \tag{2.28}$$

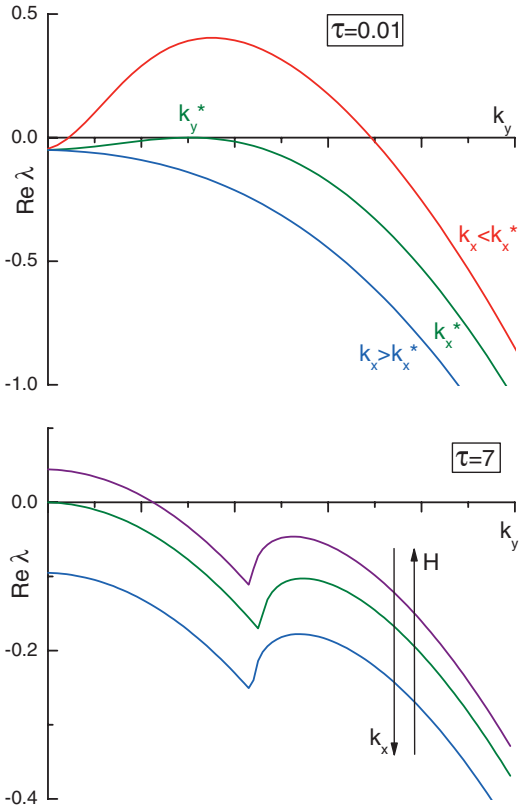

Fig. 2.6: Solutions of dispersion equation (2.26) for small and large τ, for $\alpha = 0.001$ and n=20.

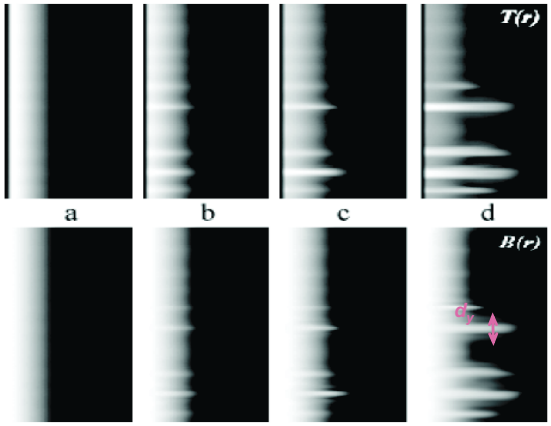

Fig. 2.7: Evolution of the temperature and flux density distributions (white color) produced by simulations. The instability is triggered by applying a magnetic field [42].

Here $H_{\rm adiab}^{\rm slab}$ is the adiabatic instability field for the slab geometry [25–28, 36]. This result coincides up to a numerical factor with the adiabatic instability field for a thin strip found recently in Ref. [41].

Solutions of Eq. (2.26) for perturbations with arbitrary k_y are presented in Figure 2.6. The upper panel shows $\mathrm{Re}\,\lambda(k_y)$ curves for $\tau = 0.01$ and different values of k_x. For large k_x, i. e., small magnetic field, $\mathrm{Re}\,\lambda$ is negative for all k_y. It means that the superconductor is stable. However, at small k_x, the increment $\mathrm{Re}\,\lambda$ becomes positive in some finite range of k_y. Hence, some perturbations with a spatial structure will start growing. They will have the form of fingers of elevated T and E directed perpendicularly to the flux front. We will call this situation the *fingering (or dendritic) instability.*

Simulations (Figure 2.7) showing step-by-step development of fingering instability was obtained by my co-authors in their early work [42]. It is seen how magnetic field starts to penetrate superconductor with smooth front, but then some fingers begin to form. Eventually dendrites develop from these initial fingers.

For large τ an instability also develops at small k_x, however in a different manner, see Figure 2.6 (lower panel). Here the maximal $\mathrm{Re}\,\lambda$ always corresponds to $k_y = 0$. Hence, the uniform perturbation will be dominant. The uniform growth of perturbations for

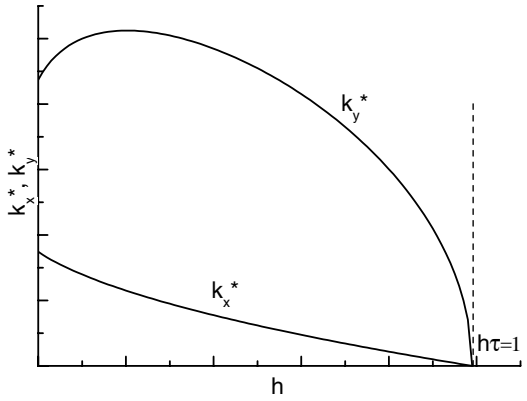

Fig. 2.8: Dependencies of k_y^* and k_x^* on h for n=20, $\tau = 0.01$, $\alpha = 0.001$ according to Eq. (2.29).

large τ has been recently predicted in [30, 35] and explained by the prevailing role of heat diffusion.

Let us now find the critical k_y^* and k_x^* for the fingering instability, see Figure 2.6 (upper panel). The k_x^* determines the applied magnetic field when the instability first takes place, while k_y^* determines its spatial scale. These quantities can be found from the requirement $\max\{\mathrm{Re}\,\lambda(k_y)\} = 0$ for $k_y \neq 0$. In the limit $\alpha \ll 1$ we can put $A_1 = 0$ in Eq. (2.26) and then rewrite it in the form

$$\lambda = -(k_y^2 + h)\tau + \frac{(k_y^2 - k_x^2)}{k_y^2 + nk_x^2}\,.$$

From this expression we obtain

$$\begin{aligned} k_x^* &= \left(\sqrt{n+1} - \sqrt{nh\tau}\right)/n\sqrt{\tau}\,, \\ k_y^* &= \left[\sqrt{nh\tau+1}\left(\sqrt{n+1} - \sqrt{nh\tau+1}\right)\right]^{1/2}/\sqrt{n\tau}\,. \end{aligned} \tag{2.29}$$

The dependencies of k_x^*, k_y^* on the heat transfer coefficient h are shown in Figure 2.8. One can see that k_y^* is always larger than k_x^* implying that fingers of elevated T and E are extended in the direction normal to the film edge. For $h \ll 1/\tau$ and $n \gg 1$ we find $k_y^* \approx n^{1/4} k_x^* \gg k_x^* \approx 1/\sqrt{n\tau}$. Both k_x^* and k_y^* tend to zero as $h \to 1/\tau$, while for larger h the system is always stable due to fast heat removal to the substrate. It

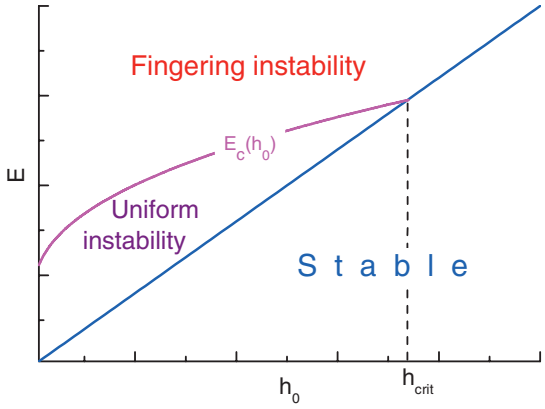

Fig. 2.9: Stability diagram in the plane electric field – heat transfer coefficient according to equation (2.31) and condition $1 - h\tau > 0$ for $n = 30$ and $\alpha = 0.001$.

follows from Figure 2.6 that for large enough τ the instability will develop uniformly, while for small τ it will acquire a spatially-nonuniform structure. Let us find now the critical value τ_c that separates these two regimes. It can be obtained from the equality $\mathrm{Re}\,\lambda(k_x = k_x^*, k_y = 0) = 0$. When it is fulfilled $\mathrm{Re}\,\lambda = 0$ both for $k_y = 0$ and for $k_y = k_y^* \neq 0$. We find using Eq. (2.26) that the instability will evolve in a spatially-nonuniform way if

$$\tau < \tau_c = \left(1 - k_x^{*2}/\gamma\alpha\right)/h\,. \tag{2.30}$$

Substituting here α and k_x^* we find a transcendental relation between τ_c and h. For $n \gg 1$ it reduces to

$$\sqrt{n\tau_c}\left(1 + \sqrt{h\tau_c}\right) = \pi a/\gamma d\,. \tag{2.31}$$

Using this result we can construct a stability diagram in the $E - h_0$ plane shown in Figure 2.9. The curved line marks the critical electric field $E_c(h_0)$ that separates two types of instability: fingering ($E > E_c$) and uniform ($E < E_c$). This line is calculated from Eq. (2.31), where the electric field is expressed via τ as $E = j_c\mu_0\kappa/nC\tau$ according to equations (2.5) and (2.6). The straight line is given by the condition $h\tau = 1$. Below this line the superconductor is always stable, as follows from Eq. (2.27) for the uniform perturbations, and from Eq. (2.29) for the nonuniform case. At a certain value

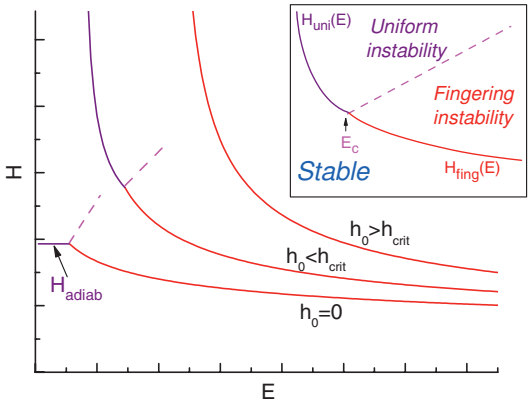

Fig. 2.10: Stability diagram in the H-E plane according to Eq. (2.27) and Eq. (2.29).

$h_0 = h_{\rm crit}$, the two lines intercept. We find

$$h_{\rm crit} = \frac{2\gamma^2\mu_0^2 j_c^4 d^3 \kappa n}{\pi^2 T^{*2} C^2}\,, \tag{2.32}$$

and the critical electric field E_c for $h_0 = 0$ is

$$E_c(0) = \frac{\gamma^2\mu_0^2 \kappa j_c^3}{\pi^2 C^2 T^*}\, d^2\,, \tag{2.33}$$

while $E_c(h_{\rm crit}) = 4E_c(0)$.

For any point (h_0,E) belonging to the stable phase in the stability diagram, Figure 2.9, the flux distribution is stable for any applied magnetic field. For the points belonging to unstable phases, the instability develops above some threshold magnetic field, either $H_{\rm fing}(h_0, E)$ or $H_{\rm uni}(h_0, E)$ for fingering or uniform instability, respectively. Shown in Fig. 2.10 are three sets of $H_{\rm fing}(E)$ and $H_{\rm uni}(E)$ curves for different values of h_0. They represent boundaries between the three phases, stable and unstable with respect to either fingering or uniform instability, as shown in the inset. Using Eq. (2.7) one can rewrite the expression Eq. (2.27) for $H_{\rm uni}$ as

$$H_{\rm uni} = H_{\rm adiab}\left(1 - \frac{2T^* h_0}{nd\, j_c E}\right)^{-1/2}\,. \tag{2.34}$$

In the absence of heat removal to the substrate, $h_0 = 0$, we obtain the adiabatic instability field, Eq. (2.28), and the $H_{\rm uni}(E)$ curve becomes a horizontal line.

Strictly speaking $H_{\rm uni}$ should increase at very small E the same way it does in bulk superconductors [25, 35]. This behavior is not reproduced in our model since we neglected the heat flow in the x direction. This flow becomes important only in the limiting case $h_0 \to 0$. In practice, the heat removal from a thin film to the substrate usually dominates the lateral heat diffusion in the film.

The threshold magnetic field for the *fingering* instability $H_{\rm fing}$ is calculated from Eq. (2.29). A simplified expression obtained for $h \ll 1/\tau$ and $n \gg 1$,

$$H_{\rm fing} = \left(\frac{j_c d^2}{\pi w} \sqrt{\frac{\kappa T^* j_c}{E}} \right)^{1/2} , \tag{2.35}$$

shows that at large electric fields $H_{\rm fing}$ decays as $E^{-1/4}$. At $h_0 \le h_{\rm crit}$ the curves $H_{\rm fing}(E)$ and $H_{\rm uni}(E)$ intercept at the critical electric field E_c determined by Eq. (2.30). At $h_0 \ge h_{\rm crit}$ we have $H_{\rm fing}(E) < H_{\rm uni}(E)$ for any E, so the lines do not intercept and the instability will develop into a fingering pattern.

2.7 Comparison with experiment

Let us compare the present results for a *thin film* in a perpendicular magnetic field with results of [35] for a *bulk* superconductor. In both cases the instability develops into a fingering pattern if the background electric field in the superconductor exceeds some critical value E_c. The values of E_c are however different. Their ratio for a thin strip and a slab,

$$\frac{E_c(0)}{E_c^{\rm slab}} = \frac{\gamma^2}{\pi^2} \, \frac{d^2 j_c^2 \mu_0}{C T^*} , \tag{2.36}$$

is expected to be much less than unity. For $j_c = 10^{10}$ A/m^2, $C = 10^3$ J/Km^3, $\kappa = 10^{-2}$ W/Km, $T^* = 10$ K and $d = 0.3\,\mu$m, we find from Eq. (2.33) that $E_c \approx 4 \cdot 10^{-4}$ V/m, while according to [35], $E_c^{\rm slab} = 0.1$ V/m. Consequently, the development of thermomagnetic instability into a fingering pattern is much more probable in thin films than in bulk superconductors.

The threshold *magnetic* field for the fingering instability $H_{\rm fing}$ is also much smaller for thin films. Comparing Eq. (2.35) with the results for a slab [35] we find

$$\frac{H_{\rm fing}}{H_{\rm inst}^{\rm slab}} = \frac{\sqrt{2}}{\pi} \frac{d}{\sqrt{w l^*}} . \tag{2.37}$$

Here $l^* = (\pi/2)\sqrt{\kappa T^*/j_c E}$ is the flux penetration depth at the threshold of the fingering instability, $H = H_{\rm fing}$. Experimentally, the fingering instability always starts after the flux has penetrated a noticeable distance from the edges, such that $l^* \gg d$ [3–15,33,34]. Hence, for a thin film the fingering instability should start at much smaller applied fields than in bulk samples (by a factor of $\sim 10^3$ for films with $d \sim 10^{-4}w$). The difference between the threshold fields for the two geometries here is even stronger than for the case of uniform instability in the adiabatic limit, see Eq. (2.28). Assuming the above values of parameters and $w = 2$ mm we find from Eq. (2.35) that $H_{\rm fing}[E_c(0)] = H_{\rm adiab} \approx 1$ mT. This value becomes larger if we take into account the heat transfer to the substrate. It is therefore in excellent agreement with experiment, [4, 6–8, 10, 12, 14, 41] where the threshold field is typically of the order of a few milliTesla.

The spatial structure of the instability predicted by our linear analysis is a periodic array of fingers perpendicular to the film edge. Its period can be estimated from Eq. (2.29). For $E = E_c$, $h = 0$ and $n \gg 1$ one finds

$$d_y = \frac{\pi^2 C T^*}{2\gamma n^{1/4} \mu_0 j_c^2 d}\,, \tag{2.38}$$

which yields $d_y \approx 100$ μm for $n = 30$. Numerical analysis of the instability development shows [30,35] that beyond the linear regime the periodic structure is destroyed and only one (strongest) finger invades the Meissner region. This scenario is indeed reproduced experimentally, and the observed width of individual fingers, 20-50 μm, [3–5,14] is very close to our estimate, $d_y/2$.

The finger width and the threshold magnetic field also depend on the dimensionless parameter h characterizing the thermal coupling to the substrate, Eq. (2.17). In turn, h, grows rapidly with temperature because of a strong T dependence of C and j_c. One can therefore make several testable predictions from the dependencies $k_x^*(h)$ and $k_y^*(h)$ shown in Figure 2.8: (i) There must be a threshold temperature $T_{\rm th}$ above which the instability is not observed. (ii) When approaching $T_{\rm th}$, the instability field diverges since $k_x^* \to 0$. (iii) When approaching $T_{\rm th}$ the characteristic width of individual fingers increases since $k_y^* \to 0$. All these predictions will be proven in later sections of the this Chapter when we introduce temperature dependencies into our equations. The last prediction has also been obtained in the boundary layer model allowing calculation of

the exact finger shape [31]. The first and the second predictions have already been confirmed experimentally [5, 12]. There is a solid experimental evidence [4, 5, 7, 12] for an enhanced degree of branching as $T \to T_{\rm th}$ that can be quantitatively described as a larger fractal dimension of the flux pattern [7]. This abundant branching could be an indirect consequence of the increased finger width since wider fingers are presumably more likely to undergo splitting.

The present problem of fingering instability in a thin film has two new features compared to a similar problem for a bulk superconductor, (i) nonlocal electrodynamics and (ii) thermal coupling to the substrate. The nonlocality results in much smaller values of the threshold magnetic field $H_{\rm fing}$ and the critical electric field E_c in films than in bulks. If a film is made thinner, it becomes even more unstable since $H_{\rm fing} \propto d$, and has a stronger tendency to form a fingering pattern since $E_c(0) \propto d^2$. The thermal coupling to the substrate has a somewhat opposite effect. It can lead to an ultimate stability if $h > 1/\tau$ – a situation that is never realized in bulks. A moderate coupling, $h \ll 1/\tau$, slightly renormalizes $H_{\rm fing}$ and E_c, i.e. makes the film a little bit more stable and less inclined to fingering.

Let us now compare the results presented in this work to those obtained in a similar model by Aranson *et al* [30]. Our expressions for the "fingering" threshold field , Eq. (2.35), and for the finger width, Eq. (2.38), agree with their results up to a numerical factor. For $\tau \gg 1$ our results for the "uniform" threshold field (derived from Eq. (2.27)) are also similar to results of [30]. As a new result, we find that there exists a critical value of the parameter τ, Eq. (2.30), which controls whether the instability evolves either in the uniform, or in the fingering way. Shown in Figure 2.9 is the stability diagram where the line $E_c(h_0)$ separates regimes of fingering and uniform instability. Other new results of this paper are: (i) the existence of a field-independent "critical point", $h_{\rm crit}$, such that for $h_0 > h_{\rm crit}$ the instability *always* develops into a fingering pattern, and (ii) the full stability diagram in the H-E plane, Figure 2.10, containing all three phases.

The background electric field needed to nucleate the fingering instability can be induced by ramping the magnetic field, $E \sim \dot{H} l \propto \dot{H} H^2$ for $l \ll w$, where $\dot{H}$ is the

ramp rate. This is the lowest estimate since the flux penetration in practice is strongly nonuniform in space and in time, [43] and there can be additional sources of E due to random fluctuations of superconducting parameters. The occurrence of the fingering instability even at rather low ramp rates [4, 6–10, 12, 14, 33] is therefore not surprising.

The build-up time of the instability can be estimated as $t_0 \approx 0.1\mu$s if the flux-flow conductivity $\sigma = 10^9\ \Omega^{-1}m^{-1}$. Our linear analysis assumes that the perturbations of T and E grow in amplitude, but remain localized within the initial flux penetrated region. Numerical results show [30, 35] that at $t \gg t_0$ the perturbations also propagate into the Meissner region. This propagation can be described by recent models [32, 44] that predict a characteristic propagation speed in agreement with experimental values of 10-100 km/s [3, 11].

2.8 Specific experiments on thin-films

To further check the validity of purposed model several experiments were specifically designed. Thin films of MgB_2 were fabricated by a two step process [45], where first a film of amorphous boron was deposited on an Al_2O_3 $(1\bar{1}02)$ substrate using a pulsed laser. The B film and high-purity Mg were then put into a Nb tube, which was sealed in a high purity Ar atmosphere and post-annealed at 900°C. To eliminate possible contamination with oxygen, water, and carbon, the samples were not exposed to air until the final form of the film was produced. The MgB_2 films possess c-axis orientation, as confirmed by scanning electron microscopy, and magnetization data show a sharp superconducting transition at 39 K. The film thickness was 300 nm.

A set of eight MgB_2 film samples was shaped by photo-lithography into 3 mm long rectangles having different widths ranging from 0.2 mm to 1.6 mm. All the samples were made from the same mother film, allowing simultaneous and comparative space-resolved magnetic observation. An additional 5 mm wide sample was made using the same preparation conditions. A standard MO imaging setup with crossed polarizers and a ferrite garnet indicator was used to visualize flux distributions.

In principle, having several superconducting samples next to each other leads to

crosstalk, i.e., field expelled by one enhances the field experienced by another. This is a price to pay for being able to make direct comparative observations. Our distance between the strips was sufficiently large, as clearly seen from Figure 2.11 where flux penetrates each strip equally from both sides. Had crosstalk been important, substantial asymmetry would be visible, especially in the upper sample having a neighbor only on one side.

Shown in Figure 2.11 is the flux penetration pattern when the eight samples, initially zero-field-cooled to 4 K, were exposed to a perpendicular applied magnetic field slowly ramped to 15 mT. The magnetic flux enters the superconductor in a form very much dominated by abrupt dendritic avalanches, although quite differently for the various samples. It is evident that the number of dendrites, their size and branching habit depend strongly on the sample width. Whereas the wide strips become densely filled with flux dendrites, the more narrow samples contain fewer, until at the 0.2 mm wide strip flux dendrites almost never appear.

This qualitative result, was followed up by measuring how the instability threshold field $H_{\rm fing}$ depends on the strip width. Results obtained for all eight strips are shown in Figure 2.12, where each data point represents an average over 4 repeated experiments using identical external conditions. The error bars indicate the scatter in the observed $H_{\rm fing}$. A variation as much as 30% implies that the nucleation of this instability is strongly affected by random processes, which is also consistent with earlier experiments [4, 5, 7, 8, 10, 12]. Nevertheless, the data in Figure 2.12 show a clear increase in the threshold field as the strip becomes narrower. In other words, reducing the sample width increases the stability of the superconductor.

Measurements of the temperature dependence of $H_{\rm fing}$ are shown in Figure 2.13. One sees that $H_{\rm fing}$ not only increases with temperature, but appears to diverge at a certain temperature. Above this threshold temperature, $T_{\rm th}$, found to be close to 10 K for MgB_2 films, the dendritic instability disappears entirely. Included in the figure are also data we have extracted from a previous MO investigation of dendritic flux penetration in Nb films [12]. The two behaviors show remarkable similarities, although with different threshold temperatures, approximately 6 K in the Nb case.

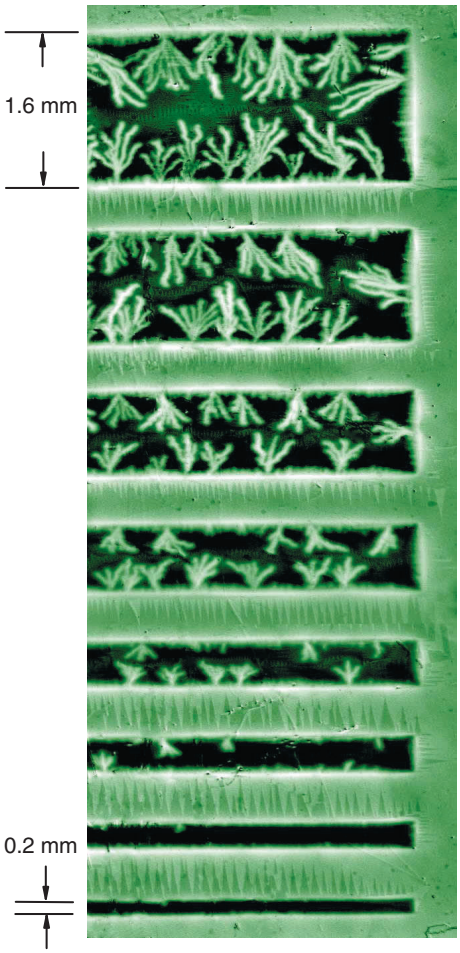

Fig. 2.11: MO image showing flux distribution in MgB_2 strip-shaped samples at 4 K and 15 mT applied field. The image brightness represents the local flux density. Both the number and size of the dendrites are larger for the wider samples.

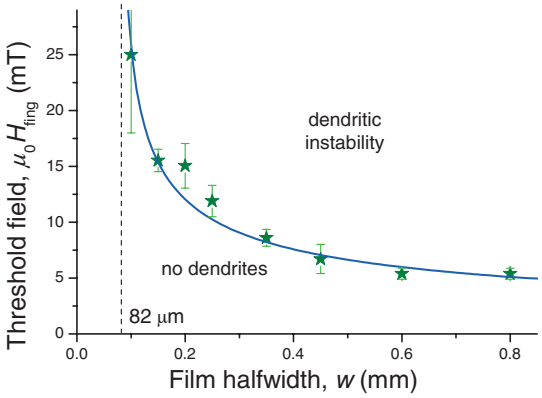

Fig. 2.12: Threshold magnetic field for onset of the dendritic instability in MgB_2 strips of different width (symbols) plotted together with a fitted theoretical curve (full line), which diverges at a finite w indicated by the dashed asymptote.

2.9 Temperature dependencies

To explain these observations we further develop the model of thermomagnetic instabilities (Paper 1). The threshold flux penetration depth, ℓ^*, when the superconducting strip first becomes unstable, is given by Eq.(2.29), which can be expressed as

$$\ell^* = \frac{\pi}{2}\sqrt{\frac{\kappa}{|j_c'|E}}\left(1-\sqrt{\frac{2h_0}{nd|j_c'|E}}\right)^{-1}. \tag{2.39}$$

Here we used equations (2.5), (2.6) and relation $\ell = \pi/2k_x$. We also introduced here j_c' as the temperature derivative of the critical current density. Approximation $n \gg 1$ was used which characterizes the strongly nonlinear current-voltage curve of the superconductor, described by the commonly used relation for the electrical field, $E \propto j^n$.

To obtain more accurate results we replace equation (2.7) with exact expression for the flux penetration depth of a long thin strip in a perpendicular applied field [39, 40]:

$$\ell = \left(1-\frac{1}{\cosh(\pi H/j_c)}\right) w \tag{2.40}$$

By combing equations (2.39) and (2.40) we obtain the threshold field, $H_{\rm fing}$:

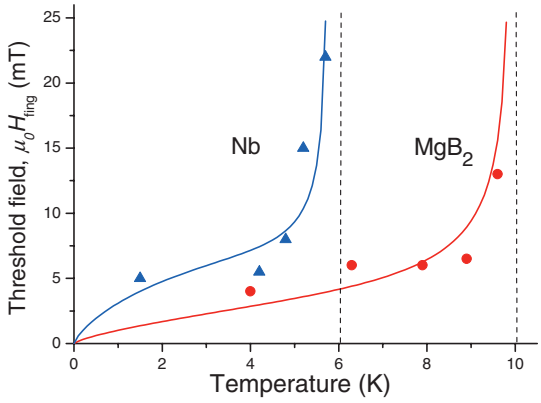

Fig. 2.13: Temperature dependence of the threshold magnetic field. Experimental data obtained for the 5 mm wide MgB_2 sample and for a 1.8 mm wide Nb film [12] are plotted as • and ▲, respectively. The full lines are theoretical fits. The dashed lines show the limiting temperature above which the instability vanishes.

$$H_{\text{fing}} = \frac{j_c d}{\pi} \operatorname{arccosh}\left(\frac{w}{w-\ell^*}\right). \tag{2.41}$$

Plotted in Figure 2.12 as a solid line is function (2.41) using $j_c = 9 \times 10^{10}$ A/m^2, a value obtained for MgB_2 at 4 K by extrapolation of $j_c(T)$-curves measured under the stable conditions above T_{th}. The only adjustable parameter, ℓ^*, was chosen equal to 82 μm, which gives an excellent agreement with our data. It follows from Eq. (2.41) that narrower strips need a larger field to reach the critical penetration depth ℓ^*, which is exactly what we find experimentally. Furthermore, the model predicts that H_{fing} should diverge when the strip halfwidth decreases towards $w = \ell^*$, also this fully consistent with our MO observations.

To fit the data observed on Figure 2.13 $H_{\text{fing}}(T)$ one needs temperature dependent model parameters. We assume then a cubic dependence of the thermal conductivity, $\kappa = \tilde{\kappa}\,(T/T_c)^3$, as suggested by low-temperature data for MgB_2 [46]. Similarly, a cubic dependence of the heat transfer coefficient, $h_0 = \tilde{h}_0\,(T/T_c)^3$ is chosen in accordance with the acoustic mismatch model confirmed experimentally for many solid-solid interfaces [47]. Furthermore, we assume a linear temperature dependence for the critical

current density, $j_c = j_{c0}(1 - T/T_c)$, and with a pinning potential, $U \propto 1 - T/T_c$, the exponent $n \sim U/kT$ also becomes T-dependent, $n = \tilde{n}\,(T_c/T - 1)$:

$$\begin{aligned} \kappa &= \tilde{\kappa}\,(T/T_c)^3\,, \\ h_0 &= \tilde{h}_0\,(T/T_c)^3\,, \\ j_c &= j_{c0}(1 - T/T_c), \\ n &= \tilde{n}\,(T_c/T - 1) \end{aligned} \tag{2.42}$$

Combining all these temperature dependencies into equation (2.41), one obtains a theoretical $H_{\text{fing}}(T)$, and such curves fitted to experimental data for MgB_2 and Nb films [12] are shown in Figure 2.13. MgB_2 data are presented for the largest (5 mm wide) film since here the instability is observed in the broadest temperature range. The model clearly reproduces the two key features; (i) the existence of a threshold temperature T_{th} above which the instability is absent, and (ii) a steep increase of the threshold field H_{fing} when T approaches T_{th}. For MgB_2 the fit was made with $j_{c0} = 10^{11}$ A/m^2, and $\tilde{\kappa} = 160$ W/Km [46], and choosing $\tilde{n} = 10$ corresponding at $T = 10$ K to the commonly used $n = 30$. The remaining parameters are the electric field and the heat transfer coefficient, where best fit was obtained with $E = 30$ mV/m and $\tilde{h}_0 = 17$ kW/Km^2. It should be emphasized that the experimental data for both $H_{\text{fing}}(w)$ and $H_{\text{fing}}(T)$ were fitted using the same parameter values, and in both cases giving excellent quantitative agreement. Figure 2.13 also shows a similar fit for the data obtained for Nb, using $T_c = 9.2$ K, $j_{c0} = 10^{11}$ A/m^2, $w = 0.9$ mm, $d = 0.5$ μm, [12] $\tilde{\kappa} = 120$ W/Km, [48] $\tilde{n} = 40$, $E = 200$ mV/m and $\tilde{h}_0 = 36$ kW/Km^2. Again the model excellently describes the experimental behavior.

The fitted electric fields represent upper limiting values, since we used bulk values for thermal conductivity, which in general are larger than for films. Nevertheless, both values largely exceed the estimate, $E \sim \dot{H}\ell^*$, expected for a uniform and gradual flux penetration with a ramp rate of $\dot{H} \approx 1$ mT/s as used in the experiments. We believe this discrepancy is due to the fact that local, rather than global, conditions govern the onset of the instability. Assuming that the flux dendrites are nucleated by abrupt microscopic avalanches of vortices [43], local short-lived electric fields can easily reach

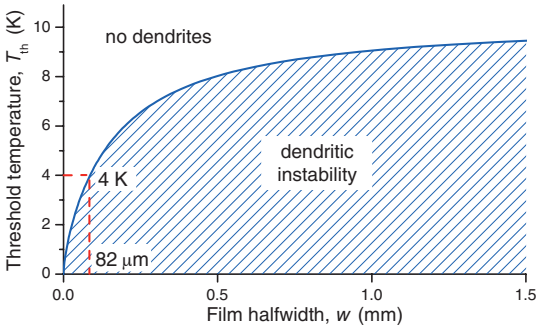

Fig. 2.14: Theoretical stability diagram predicting the threshold temperature $T_{\rm th}$ for different film width. The curve is plotted for parameter values corresponding to MgB_2 films.

those high values. In fact, such avalanches consisting of $10^2 - 10^4$ vortices occurring in an area of ~ 20 μm were recently observed by high-resolution MO imaging in MgB_2 films [41]. Electric fields close to 30 mV/m would be created if such avalanches occur during a time span of the order of 10^{-5} seconds. Randomness in such avalanches may also explain the large scatter of the observed $H_{\rm fing}$ values. We also note that the estimated electric field at the *nucleation* stage is still much lower than E values at the tip of an already *propagating* dendrite [44]. This fact is in agreement with expectations.

Finally, we emphasize that the two functions $H_{\rm fing}(w)$ and $H_{\rm fing}(T)$ have a similar feature, namely a divergence at some value of the argument beyond which the system becomes stable, see Figure 2.12 and Figure 2.13. These stability thresholds are actually related to each other by the condition $\ell^*(T_{\rm th}) = w$. The relation between the threshold temperature and the strip width is shown in Figure 2.14, and represents the stability diagram in $w - T$ coordinates, here plotted for parameters valid for MgB_2. It follows from the model that the temperature range of the instability increases monotonously with the strip width, but is limited upwards by a temperature close to 10 K for large-size films, as confirmed by many previous experiments [5, 10, 14–16]. More over instability at the given temperature may be suppressed by making samples narrow enough. For example for MgB_2 at temperatures around 4 K the width of the sample must be around

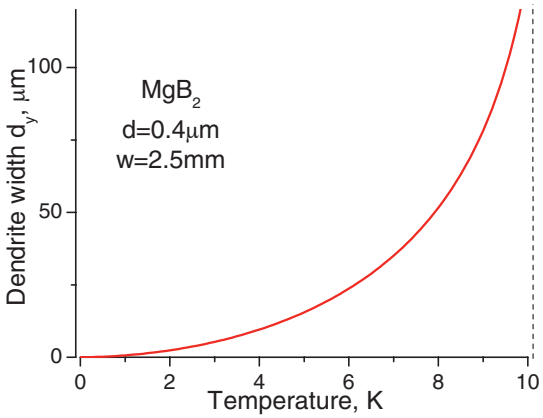

Fig. 2.15: Dependence of the dendrite width (2.43) on the background temperature.

150 μm or less to completely suppress thermomagnetic instabilities (Figure 2.14).

Another interesting result can be obtained if we substitute all temperature dependencies in the expression (2.30) for k_y as we did this for k_x (2.29). k_y corresponds to the width of the dendrite in the same way as k_x corresponds to penetration depth ℓ:

$$d_y = \frac{\pi}{2} \frac{a\sqrt{n\tau}}{(\sqrt{nh\tau+1}(\sqrt{n+1}-\sqrt{nh\tau+1}))^{1/2}} \tag{2.43}$$

To be more precise d_y corresponds to the dendrite's halfwidth as was initially shown with help of equation (2.38). Substituting into (2.43) equations (2.5), (2.6) along with temperature dependencies (2.42) we can show the growth of dendrite width with temperature (Figure 2.15).

Due to its complexity the formula corresponding to curve on Figure 2.15 is not shown. However it is seen that with increasing background temperature dendrite's size also increases. The largest dendrites will be for temperature around 10K, but experimentally it will be nearly impossible to observe because threshold magnetic field needed to achieve such instability tends to infinity. Divergence of the d_y curve near threshold temperature also suggest that development of narrow finger-like instability is not favorable in such conditions.

It is also interesting to analyze changing of dendrites properties with decreasing film thickness (as thinner samples more unstable). We again substitute all dependencies

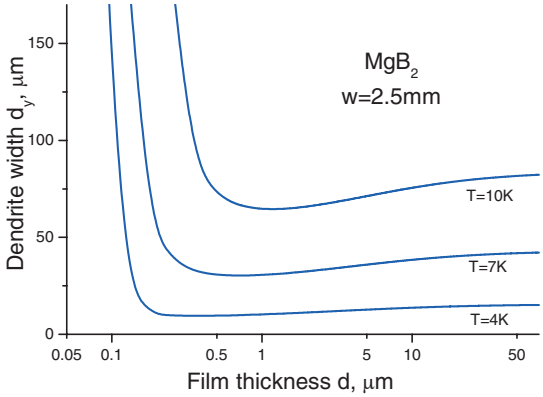

Fig. 2.16: Dependence of the dendrite width (2.43) on film thickness.

into formula (2.43), but this time we plot graph for d_y depending on thickness d (see Figure 2.16).

It is seen that for the samples with thickness larger than 50μm dendrite width changes very slightly and tends to saturation. For very thin film ($d < 100nm$) there is the divergence of the same nature as seen on Figures 2.12, 2.13, 2.15. But experimentally it is very hard to produce the such thin films, most commonly the experimental dendrite width is corresponding to saturation limit $20-70\ \mu m$ for temperatures around $4-7\ K$. All parameters used for Figures 2.15, 2.16 are the same as for Figures 2.12, 2.13.

In the end of this chapter it is also interesting to note one recent paper about thresholds fields for thermomagnetic instabilities [49]. It was discovered the existence of upper threshold magnetic H_2^{th} (see Appendix B). For fields higher than H_2^{th} instability cease to exist, which can be used as another measure to avoid instability.

2.10 Results

The linear analysis of thermal diffusion and Maxwell equations shows that a thermomagnetic instability in a superconducting film may result in either uniform or finger-like distributions of T, E and B. The fingering distributions will be observed if the

background electric field $E > E_c$, where E_c grows with the film thickness, the critical current density, the thermal conductivity and the thermal coupling to the substrate. Due to nonlocal electrodynamics in thin films they turn out to be more unstable than bulk superconductors and more susceptible to formation of a fingering pattern. This result is presented in Paper 1.

We have showed a detailed comparison of experimental data and theoretical predictions for the dendritic flux instability in superconducting films. It was shown that a thermo-magnetic model can describe key features of the instability with an excellent quantitative agreement. This includes how the onset magnetic field for the instability H_{fing} depends on both temperature and sample size. The general result that the instability is suppressed for sufficiently narrow strips, is of particular importance for design of superconducting electronic devices or other applications making use of thin film superconductors operating at temperatures below the instability threshold value. This result is presented in Paper 2.

Here shown conditions how to avoid instability in thin film superconductors:

- The temperature should be higher threshold value T_{th} (10K for MgB_2).
- Magnetic fields should be outside critical range (lower than H_{fing} and higher than H_2^{th}).
- For temperatures lower than T_{th} instability can be suppressed by making superconducting strip sufficiently narrow (for MgB_2 sample width must be less than 150 μm).

3. FLUX IN THIN FILM RINGS

3.1 Motivation

Use of thin film superconductors integrated in nanodevices requires precise knowledge of the film behavior in the presence of both external and self induced magnetic fields. Recent experiments have shown that properly designed arrays of dots and antidots can serve as effective traps for magnetic flux [50–52]. It has also been shown that patterned superconducting films allow for the motion of magnetic vortices to be guided over the film area [53–57], opening up for a new field of physics often called fluxonics. However, at present time one of the main goal is to trap the largest possible number of flux quanta inside a hole (which is called the flux saturation number $n_{\rm film}$) thus allowing higher magnetic field to be applied.

The models for flux trapping used in past years did not take into account the precise geometry of the patterned film samples. This conventional models were based on approximations applicable either to a single vortex in an infinite film, equivalent to having a hole of zero radius (Pearl vortex [58]), or to an infinitely long hollow cylinder [59, 60]. Both geometries are far from realistic for thin film devices. However recently several works considering dynamics of vortices, current and field distributions in thin-film superconductor with finite hole have been published [61–65]. Yet the flux saturation number has not been calculated so we dedicate our work to this task.

In this chapter we examine the problem of trapped flux in a thin-film superconductor ring by solving London equations. This geometry allows one to model a realistic situation of a single anti-dot in a finite thin-film sample. We will consider the case of zero external magnetic field and show that the saturation number for a thin ring can differ significantly from that of a hollow cylinder with the same radius. The satura-

tion number for bulk samples was found using magnetic field distribution from [60]. It is reported how the difference depends on the ratio between the inner radius and the thickness of the ring, r_1/d. Including external magnetic field into calculations will not change the general picture but will overcomplicate equations so it will be omitted. These results may be interesting for some authors [51, 56, 57], who described flux distribution in thin-film superconductors with different arrays of antidots based on saturation number calculated for bulk samples [59, 60].

3.2 Calculation of current distribution

We consider a ring where the outer radius, r_2, is much larger than the inner radius r_1 (Figure 3.1). This assumption is made in order to simulate a small hole of several μm in the film sample with the size of several mm. It will be assumed that the film thickness d is negligible compared to both r_1, r_2, and the London penetration depth λ_L of the superconducting material. In order to successfully apply London equation the superconducting coherence length ξ also should be smaller than radius of the hole r_1. We focus on determining the trapped flux in the ring in a remanent state where flux due to some magnetic prehistory has been trapped in the hole. It will be assumed that vortex pinning elsewhere is absent. The self-induced magnetic field depends on the current distribution, which is determined by the amount of flux Φ trapped by the ring.

In the ring $r_1 < r < r_2$, the distributions of current density $\mathbf{j}$ and induction $\mathbf{B}$ are given by the London equation, which in terms of the vector potential $\mathbf{A}$, where $\operatorname{curl} \mathbf{A} = \mathbf{B}$, reads

$$\operatorname{curl}(\lambda_L^2 \mu_0 \mathbf{j} + \mathbf{A}) = 0\,. \tag{3.1}$$

Due to the symmetry of our problem the current and vector potential have in cylindrical coordinates only one component, $\mathbf{j} = (0, j, 0)$ and $\mathbf{A} = (0, A, 0)$, respectively. The argument of the curl-operator in Eq. (3.1) is proportional to the trapped flux Φ.

$$\mu_0 \lambda_L^2 j(r) + A(r) = \frac{\Phi}{2\pi r} \tag{3.2}$$

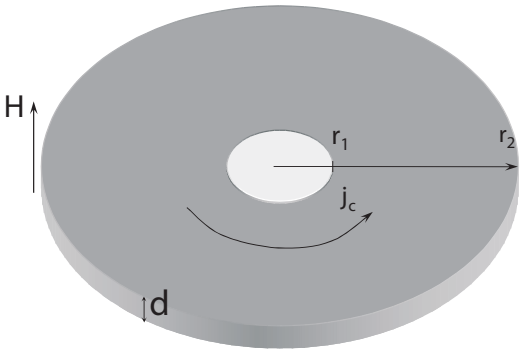

Fig. 3.1: Sketch of the thin ring geometry.

Φ here is introduced as flux free parameter which can be found from boundary conditions. We however is not interested in exact flux distribution inside the hole of the ring. For our task it is enough to know the current distribution which can be calculated using equation (3.2). Flux trapped by the ring is defined as $\Phi_{ring} = 2\pi \int_0^{r_2} \mathrm{curl}\, A(r) r dr$. The equation similar to (3.2) was analyzed in [65] in order to find the field distribution. Here we focus on the calculation of the flux saturation number.

In general case when $\lambda_L > 0$ and flux is distributed between the hole, superconducting area and outside area of the ring, the hole itself can contain fractional number of superconducting flux quanta ($\Phi_0 = h/2e$), so the number of trapped fluxes may not be integer.

Since the external field is switched off, the vector potential is only due to the current in the ring induced by the trapped flux. Thus, it can be expressed as

$$\mathbf{A} = \frac{\mu_0}{4\pi} \int \frac{\mathbf{j} \cdot d\mathbf{r}'}{|\mathbf{r} - \mathbf{r}'|} \,. \tag{3.3}$$

For the film geometry one can neglected variations of the field and current across the sample thickness and average Eq. (3.3) over z. To simplify our further equations we introduce the sheet current $I(r)$, the effective penetration depth λ_{eff} and the dimensionless variables for current $\tilde{I}$ and radius $\tilde{r}$:

$$
\begin{aligned}
I(r) &= \int_0^d j(r)dz, && (3.4)\\
\lambda_{\text{eff}} &= \lambda_L^2/d, && (3.5)\\
\tilde{I} &= (\mu_0\lambda_{\text{eff}}^2/\Phi)I, && (3.6)\\
\tilde{r} &= r/\lambda_{\text{eff}}. && (3.7)
\end{aligned}
$$

Substituting equations (3.4)-(3.7) into dependence of vector potential on current (3.3) we get our main equation to solve:

$$
\begin{aligned}
&\tilde{I}(\tilde{r}) + \frac{1}{4\pi}\int_{\tilde{r_1}}^{\tilde{r_2}}\int_0^{2\pi}\frac{\tilde{I}(\tilde{r'})\cos\theta}{\sqrt{(\tilde{r}/\tilde{r'})^2+1-2(\tilde{r}/\tilde{r'})\cos\theta}}\,d\theta d\tilde{r'}\\
&\quad = 1/2\pi\tilde{r}\,. \qquad (3.8)
\end{aligned}
$$

This Fredholm integral equation of the second kind was solved numerically by converting it into a set of linear equations corresponding to discrete values of the coordinate r:

$$
\begin{aligned}
\tilde{I}_i &+ \frac{1}{4\pi}\sum_{ij} Q_{ij}\tilde{I}_j = \frac{1}{2\pi\tilde{r}_i}, && (3.9)\\
Q_{ij} &\equiv \int_0^{2\pi}\frac{\cos\theta}{\sqrt{(\tilde{r}_i/\tilde{r}_j)^2+1-2(\tilde{r}_i/\tilde{r}_j)\cos\theta}}d\theta && (3.10)
\end{aligned}
$$

The diagonal elements of kernel (3.10) are divergent for $\theta = 0$, however after double integration of equation (3.8) the final result is finite. To get correct result during numeric calculation we had to carefully choose kernel diagonal elements. For details about numeric calculations see Appendix C. The results of the calculations are seen in the Figure 3.2, where the full curves show the radial distribution of the current for different hole sizes. These results are similar to current distributions obtained in the work of Brandt and Clem [65]. For comparison, the plot also shows (as dash-dot curve) the current distribution around a single Pearl vortex in an infinite film [58]:

$$
\tilde{I}_{\text{Pearl}}(\tilde{r}) = \left[S_1(\tilde{r}/2) - K_1(\tilde{r}/2) - 2/\pi\right]/8 \qquad (3.11)
$$

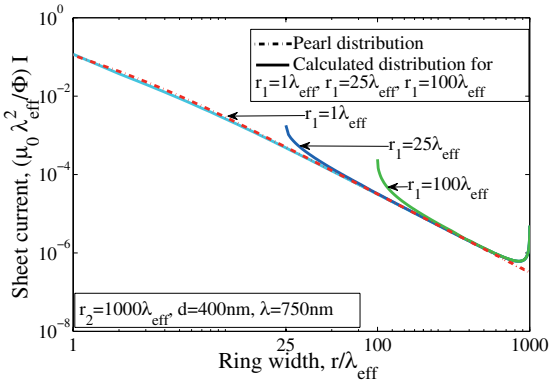

Fig. 3.2: Current distribution in superconducting thin ring. The distance is measured in λ_{eff} and the current is measured in $\Phi/\mu_0\lambda_{\text{eff}}$. There are 3 calculated current distributions corresponding to the different size of the hole: $r_1/\lambda_{\text{eff}} = 1$, 25 and 100, respectively. $r_2/\lambda_{\text{eff}} = 1000$.

Here S_1 is first order Struve function and K_1 is first order Bessel function of the second kind. For the small hole case, $r_1/\lambda_{\text{eff}} = 1$, our numerical result is almost identical to the Pearl solution, as one should expect. Obviously, our calculations must reproduce this result in the limiting case $r_1/\lambda_e \ll 1$. For the holes with $r_1 \gtrsim \lambda_{\text{eff}}$ the current profiles differ significantly from the Pearl solution in regions near both edges, where the ring solution has an upturn. All three calculated distributions have identical behavior close to the outer edge, when they begin to deviate from the Pearl solution curve. This means that for sufficiently large rings the inner edges does not influence outer edge.

Shown in Figure 3.3 is the vector potential $A(r)$ and magnetic field distribution $B(r)$ corresponding to shown current distribution. $A(r)$ and $B(r)$ were calculated using equation (3.3), relation $\mathbf{B} = \text{curl}\,\mathbf{A}$ and assuming the amount of trapped flux is equal to one quantum. (For better visualization r_2 was chosen to be equal to $4r_1$). It is seen that vector potential $A(r)$ tends to 0 when r is going to 0 or to infinity. However for the hole region the $A(r)$ distribution may not be precisely like shown in Figure 3.3 because we don't take into account exact flux distribution inside the hole. For magnetic field B the picture is different – the field generated by trapped flux is mostly concentrated

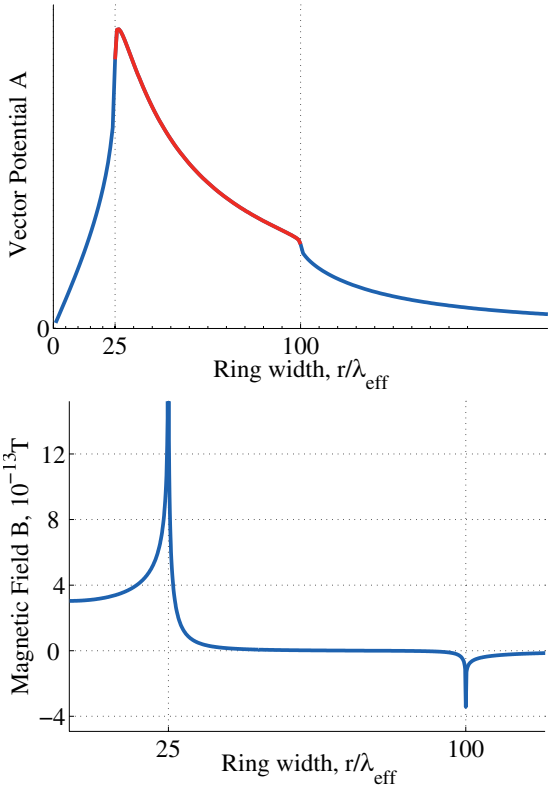

Fig. 3.3: Distribution of vector potential A and magnetic field H in the superconducting ring with one flux quanta trapped. Inner radius of the ring r_1 is equal to $25\lambda_{\text{eff}}$ and outer radius r_2 is equal to $100\lambda_{\text{eff}}$.

in the hole, while in the superconducting film it is almost completely suppressed (it decays exponentially from the edges with characteristic length λ_{eff}). Behind the outer radius of the ring B is also neglible compare to the inside region, but it should be noted that it have opposite sign there.

One more thing that will be interesting to analyze is total amount of flux trapped inside the ring. Magnetic flux trapped inside the whole ring Φ_{ring} can be calculated using vector potential $A(r)$:

$$\Phi_{ring} = 2\pi \int_0^r \operatorname{curl} A(r) r dr = 2\pi r A(r), \quad r_1 \leq r \leq r_2 \tag{3.12}$$

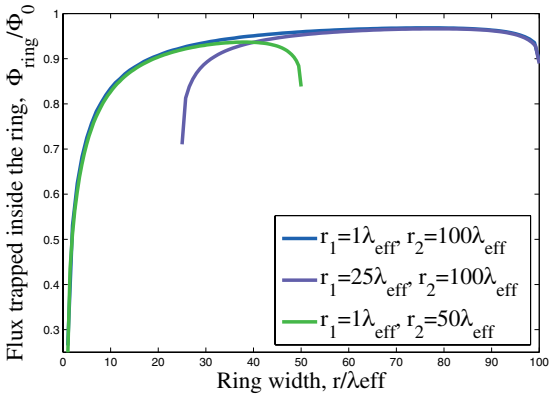

Fig. 3.4: Distribution of flux Φ_{ring} trapped inside the ring. Trapped flux is normalized to initial one flux quanta. Different curves correspond to 3 different rings: inner radius r_1 is equal to $1\lambda_{\text{eff}}$, $25\lambda_{\text{eff}}$, $1\lambda_{\text{eff}}$ and outer radius r_2 is equal to $100\lambda_{\text{eff}}$, $100\lambda_{\text{eff}}$, $50\lambda_{\text{eff}}$ correspondingly.

Shown in Figure 3.4 is the flux Φ_{ring} calculated by formula (3.12). Different lines correspond to rings with different r_1 and r_2 and the trapped flux is normalized to Φ equal to one flux quantum Φ_0. Normalized flux trapped inside the ring is always less than unity. This means that some portion of the flux escapes the ring and redistributes behind the outer radius ($r > r_2$). However flux distribution is close to initial value of $\Phi = \Phi_0$, and for $\lambda_{eff} \ll r_2$ ($r_2 \to \infty$) the trapped flux Φ_{ring} will almost equal to Φ.

3.3 Flux saturation number

Our main interest lies in finding the flux saturation number for a finite-radius hole in a thin film. Since $I \propto \Phi$ we can calculated saturation number by calculating the maximum current. We estimate the sheet current, which can flow inside the ring without destroying the superconductivity as the "depairing" current [66],

$$I_{dp} = \frac{\Phi_0 d}{3\sqrt{3}\pi\lambda_L^2\xi\mu_0}\,. \tag{3.13}$$

According to Figure 3.2 the current is maximum at the inner edge of the ring. Thus to get the saturation number n_{film} the number of trapped fluxes Φ/Φ_0 must be scaled

by factor $I_{dp}/I(r_1)$:

$$n_{\text{film}} = \frac{\Phi I_{dp}}{\Phi_0 I(r_1)} = \frac{1}{3\sqrt{3}\pi}\,\frac{1}{\tilde{I}_1}\,\frac{\lambda_{\text{eff}}}{\xi} \tag{3.14}$$

where $\tilde{I}_1 \equiv \tilde{I}(r_1)$.

It should be noted when current approaches depairing value (3.13) the superconducting order parameter is going to zero, so the actual number of quanta trapped inside the ring will be less than saturation number n_{film}. However it will not break the logic of our paper since saturation number n_{film} still corresponds to maximum possible number of trapped fluxes.

The current density is always increasing near the edges comparing to the Pearl's solution (Figure 3.2). Consequently, the actual number of fluxes trapped inside the hole of a finite size will be always less than value obtained using Pearl solution. However, for sufficiently small values of the ratio r_1/λ_{eff} the calculated values of $\tilde{I}_1$ are very close to the $\tilde{I}_{\text{Pearl}}(\tilde{r}_1)$, so we can approximate $\tilde{I}_1$ by Eq. (3.11). This expression can be further simplified in the limiting cases $r/\lambda_{\text{eff}} \ll 1$ ($\tilde{I}_{\text{Pearl}}(\tilde{r}) = 1/2\pi\tilde{r}$) and $r/\lambda_{\text{eff}} \gg 1$ ($\tilde{I}_{\text{Pearl}}(\tilde{r}) = 1/\pi\tilde{r}^2$) [58] to obtain:

$$n_{\text{Pearl}} = \frac{r}{3\sqrt{3}\xi}\begin{cases} 2\,, & r \ll \lambda_{\text{eff}}; \qquad (a) \\ r/\lambda_{\text{eff}}\,, & r \gg \lambda_{\text{eff}}. \qquad (b) \end{cases} \tag{3.15}$$

Eq. (3.15a) can be used for estimation of the flux quantity trapped inside the ring with small hole. However, in the case of a large hole the trapped flux turns to be less than that following from Eq. (3.15b). To analyze this difference we take into account the well known divergence of current distribution, $1/\sqrt{r - r_1}$, near the edge of a hole [67] and replace the Pearl's expression for $\tilde{r} \gg 1$, $\tilde{I}_{\text{Pearl}}(\tilde{r}) = 1/\pi\tilde{r}^2$, by

$$\tilde{I}_{\text{approx}}(\tilde{r}) = \frac{1}{\pi\tilde{r}\sqrt{\tilde{r}^2 - \tilde{r}_1^2}}\,. \tag{3.16}$$

Approximation (3.16) describes the current distribution very well (Figure 3.5). However it cannot be used for estimation of the current at the very edge $r = r_1$. Here we have to cut off the difference $|r - r_1|$ by λ_{eff}, so the current will be expressed as $\tilde{I}_{\text{approx}}(\tilde{r}_1) = 1/(\sqrt{2}\pi\tilde{r}^{3/2})$. Now we can finally calculate the actual saturation number for a thin ring in the large hole approximation:

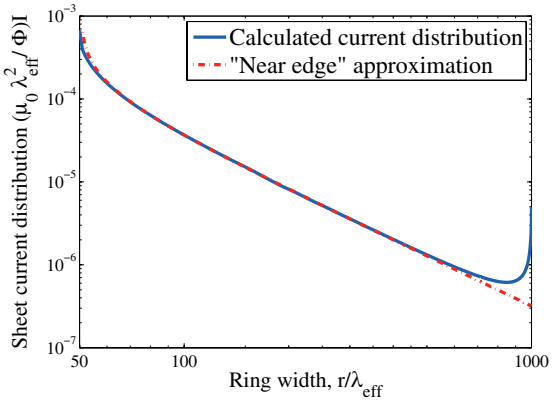

Fig. 3.5: Current distribution in superconducting thin ring. The distance is measured in λ_{eff} and the current is measured in $\Phi/\mu_0\lambda_{\text{eff}}$. The blue lines correspond to numerically calculated distribution and the red one to the "near-edge" approximation $I_{approx} = 1/\pi\tilde{r}\sqrt{\tilde{r}^2 - \tilde{r}_1^2}$. Inner radius of the ring is equal $50\lambda_{\text{eff}}$ and the outer radius is equal to $1000\lambda_{\text{eff}}$.

$$n_{\text{film}} = \frac{r_1^{3/2}}{3\sqrt{3}\xi}\sqrt{\frac{2}{\lambda_{\text{eff}}}}, \quad r \gg \lambda_{\text{eff}}\,. \tag{3.17}$$

Equation (3.17) works well for the estimation of the trapped flux, the difference between values given by this formula and numerical calculations is no more than 3% for the wide range of ratio r/λ_{eff}.

Now it will be interesting to compare the flux saturation number for a thin film and a bulk superconductor. As follows from [60], in a hollow cylinder

$$\frac{B(r')}{B_0} = \frac{K_0(r')}{K_0(r_1')}, \quad B_0 = \frac{2n_{\text{bulk}}K_0(r_1')}{\kappa r_1'[2K_1(r_1') + r_1'K_0(r_1')]}. \tag{3.18}$$

K_0 and K_1 here are zero and first order Bessels functions of the second kind.

The scaling in the Eq. (3.18) is a bit different: r' is measured in units of λ_L, B is normalized by $\Phi_0/2\pi\lambda_L\xi$, $\kappa \equiv \lambda_L/\xi$ and n_{bulk} is cavity saturation number. By taking derivative with respect to r' we can derive the current on edge of the cavity as

$$j_{\text{bulk}}(r_1') = \frac{\mu_0 n_{\text{bulk}}}{\kappa r_1'}\frac{2K_1(r_1')}{2K_1(r_1') + r_1'K_0(r_1')}\,. \tag{3.19}$$

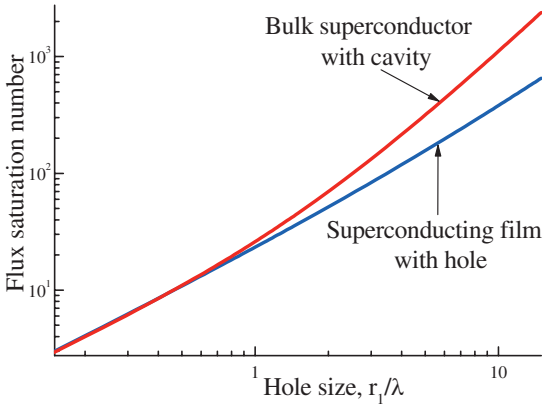

Fig. 3.6: Trapped flux inside the hole of thin superconducting film (blue line) and inside the infinite cavity in bulk superconductor (red line) depending on the size of the hole/cavity. Here values of YBaCuO film are used: $\xi = 3nm$, $\lambda_L = 150nm$, $d = 100nm$.

Using normalizing constants and putting $j_{\text{bulk}}(r_1')d$ equal to I_{dp} we can calculate the quantity of trapped flux n_{bulk}:

$$n_{\text{bulk}} = \frac{2}{3\sqrt{3}} \frac{r_1}{\xi} \left[1 + \frac{r_1}{2\lambda_L} \frac{K_0(r_1/\lambda_L)}{K_1(r_1/\lambda_L)} \right] . \tag{3.20}$$

Figure 3.6 shows the dependence of flux saturation number on the size of the hole in the ring (blue line) and infinite cavity in the bulk superconductor (red line). We used Eq. (3.14) for n_{film} calculation and Eq. (3.20) for calculations in the bulk. It is seen that a small hole can hold equal numbers of quanta in the bulk and thin films superconductor. As the size of the hole increases the curves diverge and it is obvious that thin film superconductors can trap much less flux than the bulk ones. For the limiting cases of $r_1/\lambda_L \ll 1$ and $r_1/\lambda_L \gg 1$ Bessels functions K_0 and K_1 from Eq. (3.20) can be simplified:

$$\begin{aligned} n_{bulk} &\approx \frac{2r_1}{3\sqrt{3}\xi} \left(1 + \frac{r_1}{2\lambda_L} \frac{\ln \lambda_L/r_1}{\lambda_L/r_1} \right) = \frac{2r_1}{3\sqrt{3}\xi}, \quad r_1/\lambda_L \ll 1, \\ n_{bulk} &\approx \frac{2r_1}{3\sqrt{3}\xi} \left(1 + \frac{r_1}{2\lambda_L} \frac{K_0(r_1/\lambda_L)}{K_0(r_1/\lambda_L)} \right) = \frac{r_1^2}{3\sqrt{3}\xi\lambda_L}, \quad r_1/\lambda_L \gg 1, \end{aligned}$$

$$n_{\text{bulk}} \approx \frac{r_1}{3\sqrt{3}\xi} \begin{cases} 2\,, & r_1 \ll \lambda_L \qquad (a), \\ r_1/\lambda_L\,, & r_1 \gg \lambda_L \qquad (b). \end{cases} \tag{3.21}$$

Thus, for the small hole size, the expression for the trapped flux are the same for the cases of a film and a bulk sample. For the case of large hole size the ratio $n_{\text{bulk}}/n_{\text{film}}$ is

$$\frac{n_{\text{bulk}}}{n_{\text{film}}} = \sqrt{\frac{r_1}{2d}}\,. \tag{3.22}$$

With the decreasing thickness of the film the difference between saturation numbers grows as $d^{-1/2}$. For typical parameters [50] – $d \approx 100$ nm, $r_1 \approx 500 - 600$ nm – this ratio is about 2.

3.4 Conclusion

Most important results of this chapter are presented in Paper 3. We have derived flux saturation number for the thin superconducting films with a hole of finite radius. In the limit of small hole $r_1 \ll \lambda_L$ the result is approximately equal to the flux saturation number for the bulk superconductors with a cylindric cavity of infinite height. However in the limit of large hole $r_1 \gg \lambda_L$ the hole saturation number in thin film is less that corresponding quantity in bulk superconductor by a factor $\sqrt{r_1/2d}$. Results obtained in this paper can be directly applied for a superconducting film with a single dot. Even more, knowing the exact flux saturation number, one can accurately predict vortex-dot interaction in various experimental setups with multi-dots arrays. This result promises to be of considerable importance for applications of patterned various thin-film structures, such as vortex ratchet-based rectifiers, pumps and lenses.

APPENDIX

A. PROPERTIES OF KERNEL G

A.1 Transition from Eq.(2.20) to Eq.(2.23)

The Fourier transformation for the kernel function G (2.20) with respect to variable η reads

$$G(\xi,\eta,\alpha) = \int_{-\infty}^{\infty} \frac{dk_y}{2\pi} G(\xi,k_y,\alpha) e^{ik_y\eta}\,, \tag{A.1}$$

$$G(\xi,k_y,\alpha) = \int_{-\infty}^{\infty} d\eta G(\xi,\eta,\alpha) e^{-ik_y\eta}\,, \tag{A.2}$$

Substituting Fourier transformation of kernel G into Eqs. (2.19) and (2.19), we find

$$\varepsilon_x'(\xi,k_y) = 2\alpha^2\lambda n \int_0^{\ell/a} d\xi' G(\xi-\xi',k_y)\varepsilon_x(\xi',k_y), \tag{A.3}$$

$$\varepsilon_y'(\xi,k_y) = 2\alpha^2\lambda n f(\lambda,k_y) \int_0^{\ell/a} d\xi' G(\xi-\xi',k_y)\varepsilon_y(\xi',k_y). \tag{A.4}$$

These are two linear independent integral equations with difference kernel. Each of these equations can be solved separately by a standard method.

Although the procedure of solution of Eqs. (A.3) and (A.4) is standard, we describe it in details to avoid any mistakes. In a strict sense, the symmetry of the Fourier expansions with $\cos(k_x\xi)$ and $\sin(k_x\xi)$ corresponds to the interval $-2\ell/a < \xi < 2\ell/a$ for these trigonometric functions to be orthogonal at different k_x. Thus, we should formally continue analytically $\varepsilon_{x,y}$ on this interval. These continuations are different for the sine and cosine functions. It could be easily found that the symmetry of the function $\varepsilon_y(\xi)$ corresponds to the following continuation $\widetilde{\varepsilon}_y(\xi)$ from the interval $0 < \xi < \ell/a$ to $-2\ell/a < \xi < 2\ell/a$

$$\widetilde{\varepsilon}_y(\xi) = \varepsilon_y(2\ell/a - \xi) \text{ at } \ell/a < \xi < 2\ell/a \tag{A.5}$$

and $\widetilde{\varepsilon}_y(\xi)$ is an odd function with respect to $\xi = 0$. The continuation $\widetilde{\varepsilon}_x(\xi)$ of the function $\varepsilon_x(\xi)$ is

$$\widetilde{\varepsilon}_x(\xi) = -\varepsilon_x(2\ell/a - \xi) \text{ at } \ell < \xi < 2\ell/a \tag{A.6}$$

and is even with respect to $\xi = 0$. The functions $\widetilde{\varepsilon}_{x,y}(\xi)$ coincide with $\varepsilon_{x,y}(\xi)$ at $0 < \xi < \ell/a$ and can be expanded using the same trigonometrical functions. So, we get

$$\varepsilon_x(k_x) = \frac{1}{2}\int_{-2\ell/a}^{2\ell/a} \widetilde{\varepsilon}_x(\xi)\cos(k_x\xi)d\xi = 2\int_0^{\ell/a} \varepsilon_x(\xi)\cos(k_x\xi)d\xi, \tag{A.7}$$

$$\varepsilon_y(k_x) = \frac{1}{2}\int_{-2\ell/a}^{2\ell/a} \widetilde{\varepsilon}_y(\xi)\sin(k_x\xi)d\xi = 2\int_0^{\ell/a} \varepsilon_y(\xi)\sin(k_x\xi)d\xi. \tag{A.8}$$

Let us produce a similar continuations with the function G. First, we consider $G(\xi - \xi')$ in Eq. (A.3) as a function of two independent arguments, $G(\xi, \xi')$. Then we can define the continuation $\widetilde{G}_x(\xi')$ of $G(\xi')$ as

$$\widetilde{G}_x(\xi') = -G(2\ell/a - \xi') \text{ at } \ell/a < \xi' < 2\ell/a \tag{A.9}$$

and even with respect to $\xi' = 0$. Second, in Eq. (A.4), we can define the continuation $\widetilde{G}_y(\xi')$ of $G(\xi')$ as

$$\widetilde{G}_y(\xi') = G(2\ell/a - \xi') \text{ at } \ell/a < \xi' < 2\ell/a \tag{A.10}$$

and $\widetilde{G}_y(\xi')$ is an odd function with respect to $\xi' = 0$. The functions $\widetilde{G}_{x,y}(\xi, \xi')$ obey the same symmetry with respect to the other argument ξ since $G[(\xi - \xi')]$ is symmetric with respect to a permutation of ξ and ξ' as follows from (2.19).

The integrals, Eqs. (A.3) and (A.4), can now be written as

$$\widetilde{\varepsilon}_x\,'(\xi) = \frac{\alpha^2\lambda n}{2}\int_{-2\ell/a}^{2\ell/a} d\xi'\widetilde{G}_x(\xi, \xi')\widetilde{\varepsilon}_x(\xi'), \tag{A.11}$$

$$\widetilde{\varepsilon}_y\,'(\xi) = \frac{\alpha^2\lambda n f(\lambda, k_y)}{2}\int_{-2\ell/a}^{2\ell/a} d\xi'\widetilde{G}_y(\xi, \xi')\widetilde{\varepsilon}_y(\xi'). \tag{A.12}$$

The solutions of these equations coincide with the solutions of the original Eqs. (A.3) and (A.4) at $0 < \xi < \ell/a$ and have the symmetry necessary for the suggested Fourier transformations.

Let us introduce the Fourier transformations

$$\widetilde{G}_x(\xi,\xi') = \sum_{k_x,k_x'} G_x(k_x,k_x')\cos(k_x\xi)\cos(k_x'\xi'), \tag{A.13}$$

$$\widetilde{G}_y(\xi,\xi') = \sum_{k_x,k_x'} G_y(k_x,k_x')\sin(k_x\xi)\sin(k_x'\xi'), \tag{A.14}$$

where

$$G_x(k_x,k_x') = 4\int_0^{\ell/a} d\xi \int_0^{\ell/a} d\xi' G_x(\xi,\xi')\cos(k_x\xi)\cos(k_x'\xi'), \tag{A.15}$$

$$G_y(k_x,k_x') = 4\int_0^{\ell/a} d\xi \int_0^{\ell/a} d\xi' G_y(\xi,\xi')\sin(k_x\xi)\sin(k_x'\xi'), \tag{A.16}$$

and $G_{x,y}(k_x,k_x') = G_{x,y}(k_x',k_x)$. Equations (A.15),(A.16) lead to (2.23)

A.2 Approximation of kernel G (2.20)

First, note that we do not disregard the value of the order of $(d/\ell)^2$ in the denominator of the function G (2.20). It seems as an exceeding of accuracy since previously we neglect the z dependence of electric field and temperature across the film. In other words, in the film

$$\varepsilon_i(\zeta) = \varepsilon_i(0) + \frac{\zeta^2}{2}\frac{\partial^2\varepsilon_i}{\partial\zeta^2} + \dots, \tag{A.17}$$

where the first derivative is omitted due to the symmetry. We neglect all the terms in the right hand side of Eq. (A.17), except the first. That is, we should seemingly neglect all the values of the order of $(d/\ell)^2$ and for the temperature perturbation as well. However, it is not so since the derivatives across the film thickness includes additional smallness. In the case of electromagnetic values it is due to the assumption that $d \le \lambda_L$ and for the temperature due to the smallness of Bio number $Bi = h_0 d/\kappa$ in any realistic situation for a thin film.

As in the previous study [35], we analyze here the stability in the linear approximation following two different ways. In qualitative approach, we do not specify the boundary conditions exactly assuming that k_x is of the order of a/ℓ, and analyze evolution of perturbations with each k_x independently. In this approach we evidently need only diagonal component of the kernel G with $k_x = k_x'$. If we specify the boundary

conditions and try to find exact expressions for the stability criterion and characteristic time and spatial scales, we need to know kernel function in a more general form. Both the approaches should give rise to qualitatively the same results.

A.3 Transition from Equations (2.21) and (2.23) to formula (2.25)

Performing the integration of Fourier transformation for the kernel function G (2.23) we get

$$G(\xi, k_y) = \frac{k_y a}{2\pi\ell\sqrt{\xi^2+\alpha^2}} K_1\left(k_y\sqrt{\xi^2+\alpha^2}\right), \tag{A.18}$$

where K_1 is the modified Bessel function of the second kind. In general case, the kernel function $G(k_x, k'_x, k_y)$ could not be found in the explicit form and Eqs. (2.21) and (2.22) should be solved numerically. However, we are interested here only in the specific case $\alpha \ll 1$. Within these limit the analytical expressions for the kernel can be found.

The expressions for the Fourier components of the function G read

$$G_x(k_x, k'_x, k_y) = \tag{A.19}$$
$$= \frac{2k_y a}{\pi\ell}\int_0^{\ell/a} d\xi \int_0^{\ell/a} d\xi' \frac{K_1\left[k_y\sqrt{(\xi-\xi')^2+\alpha^2}\right]\cos(k_x\xi)\cos(k'_x\xi')}{\sqrt{(\xi-\xi')^2+\alpha^2}},$$
$$G_y(k_x, k'_x, k_y) = \tag{A.20}$$
$$= \frac{2k_y a}{\pi\ell}\int_0^{\ell/a} d\xi \int_0^{\ell/a} d\xi' \frac{K_1\left[k_y\sqrt{(\xi-\xi')^2+\alpha^2}\right]\sin(k_x\xi)\sin(k'_x\xi')}{\sqrt{(\xi-\xi')^2+\alpha^2}}.$$

Under conditions specified for (A.19),(A.20), the main contribution to these integrals evidently comes from the region $|\xi - \xi'| < \alpha$. At larger $|\xi - \xi'|$ the functions under integrals decays exponentially. So, we can replace the Bessel function $K_1(x)$ under integrals by its expression at small value of argument x up to the order of x

$$K_1(x) \approx \frac{1}{x} + \frac{x}{2}\ln x \tag{A.21}$$

From Eqs. (A.19) and (A.20) we find in the main approximation accounting for the first term in the right hand side of Eq. (A.21)

$$G_x^1(k_x,k_x',k_y)=\frac{2a}{\pi\ell}\int_0^{\ell/a}d\xi\int_{-\xi}^{\ell/a-\xi}du\frac{\cos(k_x\xi)\cos[k_x'(\xi+u)]}{u^2+\alpha^2}, \tag{A.22}$$

$$G_y^1(k_x,k_x',k_y)=\frac{2a}{\pi\ell}\int_0^{\ell/a}d\xi\int_{-\xi}^{\ell/a-\xi}du\frac{\sin(k_x\xi)\sin[k_x'(\xi+u)]}{u^2+\alpha^2}, \tag{A.23}$$

where we proceed to integration over $u=\xi'-\xi$.

We need to compute following integrals, the first one for G_x^1 and the second for G_y^1:

$$\int_0^{\ell/a}\cos k_x\xi\cos k_x'\xi d\xi\int_{\xi}^{\ell/a-\xi}du\frac{\cos k_x'u}{u^2+\alpha^2}- \\ -\int_0^{\ell/a}\cos k_x\xi\sin k_x'\xi d\xi\int_{\xi}^{\ell/a-\xi}du\frac{\sin k_x'u}{u^2+\alpha^2} \tag{A.24}$$

$$\int_0^{\ell/a}\sin k_x\xi\sin k_x'\xi d\xi\int_{\xi}^{\ell/a-\xi}du\frac{\cos k_x'u}{u^2+\alpha^2}+ \\ +\int_0^{\ell/a}\sin k_x\xi\cos k_x'\xi d\xi\int_{\xi}^{\ell/a-\xi}du\frac{\sin k_x'u}{u^2+\alpha^2} \tag{A.25}$$

The calculation of this integrals are almost identical, so we show only computing of the first one. In the beginning we need to compute following integral

$$\int_{-\xi}^{\ell/a-\xi}du\,\frac{\cos k_xu}{u^2+\alpha^2}=\int_{-\xi}^{\ell/a-\xi}\frac{du}{u^2+\alpha^2}-\int_{-\xi}^{\ell/a-\xi}du\,\frac{1-\cos k_xu}{u^2+\alpha^2}\,. \tag{A.26}$$

The first integral yields $\alpha^{-1}\left[\arctan(\xi/\alpha)+\arctan(\ell/a-\xi)/\alpha\right]$. Thus we have to calculate

$$\frac{2a}{\pi\ell}\int_0^{\ell/a}d\xi\,\cos k_x\xi\cos k_x'\xi\left[\arctan(\xi/\alpha)+\arctan(\ell/a-\xi)/\alpha\right]\,.$$

One can show that off-diagonal integrals, i. e. for $k_x\neq k_x'$, are very small, and we will keep only diagonal elements which are the same for all k_x. Let us denote them as $[1-c(\alpha)]/\alpha$. For $\alpha\ll 1$ one finds $c(\alpha)\propto\alpha$, while a good approximation for $\alpha\lesssim 1$ case is $c(\alpha)\approx 1.6a^{0.84}$. Even though $c(\alpha)\to 0$ for $\alpha\to 0$ its account is important since $c(\alpha)$ will enter the dispersion law with the factor $\propto k^2$.

The second integral in Eq. (A.26) can be calculated numerically, it has the order of k_x^2, let us denote this integral as $r(\alpha,k_x)$. The values of $r(\alpha,k_x)$ in the limit $\alpha\ll 1$ depend on k_x, namely $r(\alpha,k_x)=0$ for $k_x=0$ and $r(\alpha,k_x)\to k_x$ for $k_x\gg 1$.

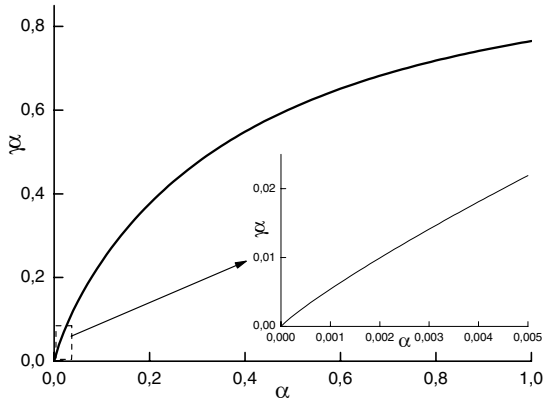

Fig. A.1: Plot of the product $\gamma\alpha$ versus α for the lowest instability mode, $k_x = \pi a/2\ell$. Shown in inset is the plot for small values of α.

To complete computation of Eqs. (A.22) and (A.23) we also need to calculate integral

$$\int_0^{\ell/a} \cos k_x\xi \sin k'_x\xi d\xi \int_\xi^{\ell/a-\xi} du \frac{\sin k'_x u}{u^2+\alpha^2}, \tag{A.27}$$

which for $k_x = (\pi a/2\ell)(2n+1)$ is equal to zero. The same results one can obtain for G^0_y. Despite the fact that Eq. (A.22) contains *cos* and Eq. (A.23) contains *sin* the final results are the same thus we employ the approximation

$$G^1_{x,y}(k_x, k_x; k_y) = \frac{a}{\ell}\left[\frac{1-c(\alpha)}{\alpha} - r(\alpha, k_x)\right] \tag{A.28}$$

Denoting $c(\alpha)/\alpha + r(\alpha, k_x)$ as $\gamma(\alpha, k_x)$ we get equation (2.25) in the main text. The dependence of $\gamma(\alpha, k_x)$ on α for the main instability mode $k_x = \pi a/2\ell$ is shown on Figure A.1.

A.4 Calculation of kernel G up to the second order

To calculate second order of kernel $G^2_{x,y}$ (2.25) we need to take into account logarithmic term when we approximate Bessel function in equation (A.21). Thus we the the following integral:

$$\frac{k_y^2 a}{\pi \ell} \int_0^{\ell/a} \cos k_x \xi d\xi \int_0^{\ell/a} d\xi \ln(k_y \sqrt{(\xi - \xi')^2 + \alpha^2}) \cos k_x' \xi' \tag{A.29}$$

To do this we have to split $\ln(k_y \sqrt{(\xi - \xi')^2 + \alpha^2})$ into $\ln(k_y) + \frac{1}{2} \ln((\xi - \xi')^2 + \alpha^2)$. The first part of integral can be solved analytically quite easily and using that $k_x = \frac{\pi a}{2\ell}(1 + 2n)$ we get following result:

$$\frac{k_y^2 a \ln k_y}{\pi \ell k_x^2} \tag{A.30}$$

The second part of integral (A.29) cannot be solved analytically. Using numerical computation for $\alpha \ll 1$ we find an approximately linear dependence of this integral on α: $a + b\alpha$. For $k_x = (\pi a)(2\ell)$ this will be $-1.386 + 3.1\alpha$. The full equation for $G_{x,y}$ will be:

$$G_{x,y}^2(k_x, k_x, k_y) = \frac{a}{\ell} \left[\frac{1 - \gamma(\alpha, k_x)\alpha}{\alpha} + \frac{k_y^2 \ln k_y}{\pi k_x^2} + \frac{k_y^2}{2\pi}(a + b\alpha) \right] \tag{A.31}$$

Using (A.31) we can get more precise equations for (2.26). The changes will be very simple - all terms containing $\gamma\alpha$ will transform into $(\gamma\alpha - \alpha \frac{k_y^2 \ln k_y}{\pi k_x^2} - \alpha \frac{k_y^2}{2\pi}(a + b\alpha))$:

$$\begin{aligned} A_1 &= n(\gamma - \frac{k_y^2 \ln k_y}{\pi k_x^2} - \frac{k_y^2}{2\pi}(a + b\alpha)\alpha \,, \\ A_2 &= k_y^2(1 + \tau A_1) + n k_x^2 + A_1(h\tau - 1) \,, \\ A_3 &= k_y^4 \tau + n k_x^2 k_y^2 \tau + n k_x^2 (h\tau + 1/n) + k_y^2 (h\tau - 1). \end{aligned} \tag{A.32}$$

B. UPPER THRESHOLD MAGNETIC FIELD H_2^{th}

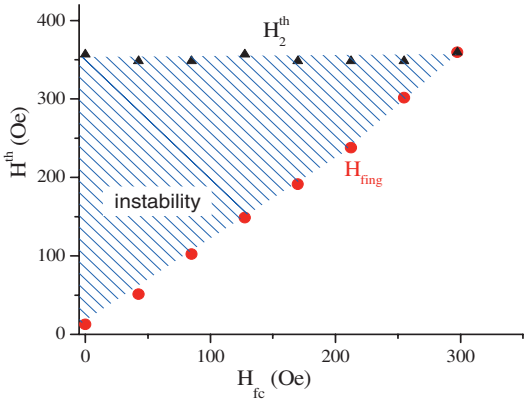

Fig. B.1: The lower and upper threshold fields $H_{\rm fing}$ (disks) and H_2^{th} (triangles) measured at different frozen-in fields after field-cooling to 4 K. For magnetic fields higher than H_2^{th} thermomagnetic instability is completely suppressed in the sample. [V. Yurchenko et al, Reentrant stability of superconducting films, cond-mat/0702683]

C. CALCULATION OF KERNEL Q_{IJ} ELEMENTS

The main problem with calculation of kernel Q_{ij} (3.10) is its diagonal elements, which are divergent for $\theta = 0$. However if we first analytically integrate kernel (3.10) over θ we get divergence in the following form:

$$Q_{\theta=0}(r, r') = C_1 + C_2 \ln(r - r') \tag{C.1}$$

C_1 and C_2 here are some yet unknown coefficients. Next we integrate equation (C.1) over $r - r'$ from 0 to $s/2$ and from 0 to $-s/2$ and normalize the answer to $s/2$ - thus we get weighted value of diagonal element. Here s is our grid step, $s = r_i - r_j$. Effectively this operation means that equation (C.1) transforms to:

$$Q_{\theta=0}(r_i, r_j) = C_1 + C_2(\ln(s/2) - 1) \tag{C.2}$$

To accurately find coefficients C_1 and C_2 we should calculate $Q_{\theta=0}(r_i, r_j)$ in several points close to $r_i = r_j$. In this work kernel values were calculated at points $r_i = r_j + s/2$, $r_i = r_j + s/4$, $r_i = r_j - s/2$, $r_i = r_j - s/4$. Doing so we can calculate two approximate values of diagonal element Q_{ii} when approaching point $r_i = r_j$ from left and right. Then we take average of this two values and find our final answer for Q_{ii}. It also should be noted that values of step s can vary depending on chosen grid for r_i and r_j. This method is not fast, because to find kernel diagonal value we should calculate equation (3.10) in four points instead of one, but it gives high accuracy (relative error is no more than 10^{-3}).

The rest non-diagonal elements were calculated in straight-forward way. The number of grid points for calculated current distribution shown in Figure 3.2 is 1000 with constant step, which gives high accuracy even in logarithmic scale.

BIBLIOGRAPHY

[1] J. G. Bednorz and K. A. Muller, Z. Phys. B **64**, 189 (1986).

[2] J. Nagamatsu, N. Nakagawa, T. Muranaka, Y. Zenitani and J. Akimitsu, Nature, **410**, 63 (2001).

[3] P. Leiderer, J. Boneberg, P. Brull, V. Bujok and S. Herminghaus, Phys. Rev. Lett. **71**, 2646 (1993).

[4] C. A. Duran, P. L. Gammel, R. E. Miller and D. J. Bishop, Phys. Rev. B **52**, 75 (1995).

[5] T. H. Johansen, M. Baziljevich, D. V. Shantsev, P. E. Goa, Y. M. Galperin, W. N. Kang, H. J. Kim, E. M. Choi, M.-S. Kim and S. I. Lee, Supercond. Sci.Technol. **14**, 729 (2001).

[6] I. A. Rudnev, S. V. Antonenko, D. V. Shantsev, T. H. Johansen and A. E. Primenko, Cryogenics **43**, 663 (2003).

[7] I. A. Rudnev, D. V. Shantsev, T. H. Johansen and A. E. Primenko, Appl. Phys. Lett. **87**, 042502 (2005).

[8] S. C. Wimbush, B. Holzapfel and Ch. Jooss, J. Appl. Phys. **96**, 3589 (2004).

[9] M. Menghini, R. J. Wijngaarden, A. V. Silhanek, S. Raedts, and V. V. Moshchalkov, Phys. Rev. B **71**, 104506 (2005).

[10] T.H. Johansen, M. Baziljevich, D.V. Shantsev, P.E. Goa, Y.M. Galperin, W.N. Kang, H.J. Kim, E.M. Choi, M.-S. Kim and S.I. Lee, Europhys. Lett. **59**, 599 (2002).

[11] U. Bolz, B. Biehler, D. Schmidt, B.-U. Runge and P. Leiderer, Europhys. Lett. **64**, 517 (2003).

[12] M. S. Welling, R. J. Westerwaal, W. Lohstroh and R. J. Wijngaarden, Physica C **411**, 11 (2004).

[13] A. V. Bobyl, D. V. Shantsev, T. H. Johansen, W. N. Kang, H. J. Kim, E. M. Choi and S. I. Lee, Appl. Phys. Lett. **80**, 4588 (2002).

[14] F. L. Barkov, D. V. Shantsev, T. H. Johansen, P. E. Goa, W. N. Kang, H. J. Kim, E. M. Choi and S. I. Lee, Phys. Rev. B **67**, 064513 (2003).

[15] Zuxin Ye, Qiang Li, G. D. Gu, J. J. Tu, W. N. Kang, Eun-Mi Choi, Hyeong-Jin Kim, and Sung-Ik Lee, IEEE Trans. Appl. Supercond. **13**, 3722 (2003).

[16] J. Albrecht, A. T. Matveev, M. Djupmyr, G. Schultz, B. Stuhlhofer and H.U. Habermeier, Appl. Phys. Lett. **87**, 182501 (2005).

[17] Eun-Mi Choi, Hyun-Sook Lee, Hyun Jung Kim, Byeongwon Kang, Sung-Ik Lee, A. A. F. Olsen, D. V. Shantsev and T.H. Johansen, Appl. Phys. Lett. **87**, 152501 (2005).

[18] J. S. Langer, Rev. Mod. Phys. **52**, 1 (1980).

[19] P. G. Saffman and G.G. Taylor, Proc. Soc. London, Ser. A **245**, 312 (1958).

[20] S. Pancheshnyi, M. Nudnova and A. Starikovskii, Phys. Rev. E **71**, 016407 (2005).

[21] P. B. Alers, Phys. Rev. **105**, 104 (1957).

[22] H. Kirchner, Phys. Lett. **26A**, 651 (1968).

[23] A.A. Polyanskii et al., Sov. Tech. Phys. Lett. **15**, 872 (1989).

[24] P. Hansen, K. Witter, and W. Tolksdorf, Phys. Rev. B **27**, 6608 (1983).

[25] R. G. Mints and A. L. Rakhmanov, Rev. Mod. Phys. **53**, 551 (1981).

[26] A. V. Gurevich, R. G. Mints and A. L. Rakhmanov, The Physics of Composite Superconductors, Begell House Inc., NY (1997).

[27] S. L. Wipf, Cryogenics **31**, 936 (1991).

[28] Martin N. Wilson, Superconducting magnets, Clarendon Press, Oxford, (1983).

[29] A. A. Abrikosov, Soviet Physics JETP **5**, 1174 (1957).

[30] I. S. Aranson, A. Gurevich, M. S. Welling, R. J. Wijngaarden, V. K. Vlasko-Vlasov, V. M. Vinokur and U. Welp, Phys. Rev. Lett. **94**, 037002 (2005)

[31] C. Baggio, R. E. Goldstein, A. I. Pesci, and W. van Saarloos, Phys. Rev. B **72**, 060503 (2005).

[32] B. Rosenstein, B. Ya. Shapiro, and I. Shapiro, Europhys. Lett. **70**, 506 (2005).

[33] M. R. Wertheimer and J de G. Gilchrist, J. Phys. Chem. Solids **28**, 2509 (1967).

[34] D. V.Shantsev, P. E. Goa, F. L. Barkov, T. H. Johansen, W. N. Kang, S. I. Lee Supercond. Sci. Technol. **16**, 566 (2003).

[35] A. L. Rakhmanov, D. V. Shantsev, Y. M. Galperin, T. H. Johansen, Phys. Rev. B **7**0, 224502 (2004).

[36] S. L. Wipf, Phys. Rev. **161**, 404 (1967).

[37] C. P. Bean, Rev. Mod. Phys. **36**, 31 (1964).

[38] W. T. Norris, J. Phys. D **3**, 489 (1970).

[39] E. H. Brandt, and M. Indenbom, Phys. Rev. B **48**,12893 (1993).

[40] E. Zeldov, J. R. Clem, M. McElfresh, and M. Darwin, Phys. Rev. B **49**, 9802 (1994).

[41] D. V. Shantsev, A. V. Bobyl, Y. M. Galperin, T. H. Johansen and S. I. Lee, Phys. Rev. B **72**, 024541 (2005).

[42] A. L. Rakhmanov, D. V. Shantsev, Y. M. Galperin, T. H. Johansen, Phys. Rev. B **70**, 224502 (2004).

[43] E. Altshuler and T. H. Johansen, Rev. Mod. Phys. **76**, 471 (2004).

[44] B. Biehler, B.-U. Runge, P. Leiderer and R. G. Mints, Phys. Rev. B **72**, 024532 (2005).

[45] W. N. Kang, Hyeong-Jin Kim, Eun-Mi Choi, C. U. Jung, and Sung-Ik Lee, Science **292**, 1521 (2001).

[46] M. Schneider, D. Lipp, A. Gladun, P. Zahn, A.Handstein, G. Fuchs, S. Drechsler, M. Ritcher, K. Muller, and H. Rosner, Physica C **363**, 6 (2001).

[47] E. T. Swartz and R. O. Pohl, Rev. Mod. Phys. **61**, 605 (1989).

[48] F. Koechlin and B. Bonin, Supercond. Sci. Technol. **9**, 453 (1996).

[49] V. V. Yurchenko, D. V. Shantsev, M. R. Nevala, I. J. Maasilta, K. Senapati, R. C. Budhani and T. H. Johansen, cond-mat/0702683.

[50] A. V. Silhanek, L. Van Look, R. Jonckheere, B. Y. Zhu,1S. Raedts, and V. V. Moshchalkov, Phys. Rev. B **72**, 014507 (2005).

[51] A. N. Grigorenko, G. D. Howells, S. J. Bending, J. Bekaert, M. J. Van Bael, L. Van Look, V. V. Moshchalkov, Y. Bruynseraede, G. Borghs, I. I. Kaya and R. A. Stradling, Phys. Rev. B **63**, 052504 (2001).

[52] G. R. Berdiyorov, M. V. Miloshevich and F. M. Peeters, Phys. Rev. B **74**, 174512 (2006).

[53] V. Yurchenko, M. Jirsa, O. Stupakov and R. Wordenweber, J. Low Temp. Phys. **139**, 331 (2005).

[54] J. Van de Vondel, C. C. de Souza Silva, B. Y. Zhu, M. Morelle, and V. V. Moshchalkov Phys. Rev. Lett. **94**, 057003 (2005).

[55] B. Y. Zhu, F. Marchesoni, V. V. Moshchalkov and F. Nori, Phys. Rev. B **68**, 014514 (2003).

[56] A. Castellanos, R. Wordenweber, G. Ockenfuss, A. v.d. Hart and K. Keck, Appl. Phys. Lett. **71**, 962 (1997).

[57] V. V. Moshchalkov, M. Baert, V. V. Metlushko, E. Rosseel, M. J. Van Bael, K. Temst, Y. Bruynseraede, and R. Jonckheere, Phys. Rev. B **57**, 3615 (1998).

[58] J. Pearl, Appl. Phys. Lett **5**, 65 (1964).

[59] G. S. Mkrtchyan and V. V. Schmidt, Sov. Phys. JETP **34**, 195 (1972).

[60] H. Nordborg and V. M. Vinokur, Phys. Rev. B **62**, 12408 (2000).

[61] J. R. Kirtley, C. C. Tsuei, V. G. Kogan, J. R. Clem, H. Raffy, and Z. Z. Li, Phys. Rev. B **68**, 214505 (2003).

[62] J. R. Kirtley, C. C. Tsuei, and F. Tafuri, Phys. Rev. Lett. **90**, 257001 (2003).

[63] A. A. Babaei Brojeny and J. R. Clem, Phys. Rev. B **68**, 174514 (2003).

[64] V. G. Kogan, J. R. Clem, R. G. Mints, Phys. Rev. B **69**, 064516 (2004).

[65] E. H. Brandt and J. R. Clem, Phys. Rev. B **69**, 184509 (2004).

[66] E. H. Brandt, Rep. Prog. Phys. **58** 1465 (1995).

[67] A. Larkin and Y. Ovchinnikov, Sov. Phys. JETP **34**, 651 (1972).